Article

Leiomodin 2 neonatal dilated cardiomyopathy mutation results in altered actin gene signatures and cardiomyocyte dysfunction

Check for updates

Jessika B. Iwanski [1], Christopher T. Pappas [1], Rachel M. Mayfield[1], Gerrie P. Farman[1], Rebecca Ahrens-Nicklas[2], Jared M. Churko [1] ✉ & Carol C. Gregorio [1,3] ✉

Neonatal dilated cardiomyopathy (DCM) is a poorly understood muscular disease of the heart. Several homozygous biallelic variants in *LMOD2*, the gene encoding the actin-binding protein Leiomodin 2, have been identified to result in severe DCM. Collectively, *LMOD2*-related cardiomyopathies present with cardiac dilation and decreased heart contractility, often resulting in neonatal death. Thus, it is evident that Lmod2 is essential to normal human cardiac muscle function. This study aimed to understand the underlying pathophysiology and signaling pathways related to the first reported *LMOD2* variant (c.1193 G > A, p.Trp398*). Using patient-specific human induced pluripotent stem cell-derived cardiomyocytes (hiPSC-CMs) and a mouse model harboring the homologous mutation to the patient, we discovered dysregulated actin-thin filament lengths, altered contractility and calcium handling properties, as well as alterations in the serum response factor (SRF)-dependent signaling pathway. These findings reveal that LMOD2 may be regulating SRF activity in an actin-dependent manner and provide a potential new strategy for the development of biologically active molecules to target *LMOD2*-related cardiomyopathies.

Dilated cardiomyopathy (DCM) is a muscle disease characterized by enlargement of the ventricular cavities of the heart, causing systolic dysfunction and impaired contractility[1–3]. Secondary effects due to compensatory neurohormonal activation can cause irreversible remodeling of the myocardium and myocyte damage[4], ultimately necessitating mechanical circulatory support and/or orthotopic cardiac transplantation. Neonatal DCM, although rare, represents the most severe form of DCM and carries a high risk of morbidity and mortality[5]. It is now estimated that approximately 40% of patients with DCM have an underlying pathogenic genetic mutation[2,6]. Thus far, >60 genes have been identified in the pathogenesis of DCM with the majority of mutations arising from proteins in the sarcomere, cytoskeleton, nuclear envelope, sarcolemma, ion channels, or intercellular junctions[3,4]. However, these genes only account for a subset of DCM cases resulting in a large gap in knowledge regarding the genetic determinants of DCM, particularly in the pediatric population.

Leiomodin (Lmod), a thin filament pointed end actin-binding protein, functions as a potent actin filament nucleator in vitro and elongation factor in myocytes[7–10]. Lmod is encoded by separate genes (*LMOD1-3*) leading to expression of three isoforms that are critical in maintaining proper muscle function[11], such that mutations in all isoforms lead to development of muscle disease. A biallelic mutation in *LMOD1*, the smooth muscle-specific isoform[12], results in megacystis microcolon intestinal hypoperistalsis syndrome[13]. Homozygous or compound heterozygous mutations in *LMOD3*, the skeletal muscle-specific isoform[14,15] result in nemaline myopathy, a disorder characterized by skeletal muscle weakness and hypotonia. *LMOD2*, which is the cardiac muscle-predominant isoform, has been implicated in severe neonatal and infantile DCM due to several homozygous loss of function variants in *LMOD2*[16–20]. This disease process has been recapitulated in *Lmod2*-KO mice as they display significantly shorter actin-thin filament lengths and die at approximately day 15 with development of

¹Department of Cellular and Molecular Medicine and Sarver Molecular Cardiovascular Research Program, University of Arizona, Tucson, AZ, 85724, USA. ²Department of Pediatrics and Division of Human Genetics and Metabolism, The Children's Hospital of Philadelphia, Philadelphia, PA, 19104, USA. ³Department of Medicine and Cardiovascular Research Institute, Icahn School of Medicine at Mount Sinai, New York, NY, 10029, USA. ✉e-mail: jchurko@arizona.edu; carol.gregorio@mssm.edu

DCM (e.g., enlarged ventricular lumens, thin ventricular walls, eccentric remodeling, and a decreased ejection fraction)[9].

Previously, we described the first disease-causing mutation in *LMOD2* in a neonate presenting with severe DCM[20]. Rapid exome sequencing identified a biallelic homozygous nonsense mutation (c.1193 G > A, p.Trp398*) in the *LMOD2* gene and explanted heart tissue demonstrated undetectable levels of LMOD2 protein, extraordinarily short actin-thin filaments, and severe reduction of maximum calcium-activated force production[20]. Several other reports further demonstrated the pathogenicity of *LMOD2* variants, collectively reporting the development of severe neonatal or infantile DCM presenting with actin-thin filament dysregulation and severe muscle weakness[16–19]. To better understand the physiological consequences of the first disease-causing mutation and LMOD2's sarcomeric function, we generated *LMOD2* W398* and isogenic control human iPSC-derived cardiomyocytes (hiPSC-CMs) and a mouse model harboring the homologous mutation to the patient (*Lmod2* W405*). We discovered structural changes at the level of the sarcomere, altered contractile properties, and compromised ability to regulate calcium flux in *LMOD2* W398* hiPSC-CMs. In parallel, homozygous *Lmod2* W405* mice demonstrated shortened actin-thin filaments and reduced force production with the development of DCM. The serum response factor (SRF) transcriptional pathway, involved in cell growth and muscle development, as well as cardiac disease progression (for review[21]), was downregulated in *LMOD2* mutant hiPSC-CMs, *Lmod2* W405* and *Lmod2*-knockout (KO) mouse models. Together, we propose that Lmod2 influences the activity of SRF through its canonical role in regulating thin filament assembly.

Results

LMOD2 W398* hiPSC-CMS express low levels of truncated LMOD2

Sequence homology and biochemical studies have revealed Lmods contain one N-terminal tropomyosin binding (Tpm) site and three actin-binding (A) sites; A1 is located after Tpm in the N-terminal half of the protein, A2 is central and comprised of a leucine-rich repeat (LRR) domain, and A3 is made up of a Wiskott-Aldrich-Syndrome protein homology 2 (WH2) domain, located near the C-terminus. The *LMOD2* p.W398* mutation (henceforth referred to as *LMOD2* W398*) is located in the C-terminal half of LMOD2 and encodes a premature termination codon that is predicted to result in a truncated ~45 kDa protein (of note, full-length LMOD2 is ~ 62 kDa). Truncation of the C-terminus of LMOD2 would lead to loss of the third actin-binding site (Fig. 1a). To determine if this mutation truly results in truncation of the LMOD2 protein, patient-specific *LMOD2* W398* hiPSC-CMs were generated along with CRISPR/Cas9 gene-edited isogenic control lines. Immunoblot analysis confirmed *LMOD2* W398* hiPSC-CMs express truncated LMOD2 protein (~ 55 kDa), albeit at very low levels (~ 3%) compared with full-length LMOD2 expression (Fig. 1b), suggesting either a low level of LMOD2 protein is expressed and/or is rapidly degraded in mutant cells.

To confirm the optimal time of performing experiments in hiPSC-CMs, the expression of LMOD2 was examined in cell culture on days 15–30 after cardiomyocyte differentiation (Supplemental Fig. 1). Immunoblot analysis of hiPSC-CMs demonstrated increasing LMOD2 expression over time (2.6-, 3.4- and 6.2-fold increase in LMOD2 expression at days 20, 25, and 30, respectively, compared to day 15). This is congruent with previous RNA-sequencing analysis of hiPSC-CMs showing increased LMOD2 expression on day 30 in culture[22]. Based on our immunoblot results, hiPSC-CMs were cultured for a minimum of 30 days prior to experimental use.

Since Lmod2 has important functions in thin filament regulation and actin dynamics, we next examined if the *LMOD2* W398* mutation alters expression of other integral sarcomeric components (Supplemental Fig. 2). Immunoblot analysis demonstrated that both thin (CAP2, Tmod1 and tropomyosin) and thick (MyBP-C and myosin) filament protein expression was not significantly different between *LMOD2* W398* hiPSC-CMs and isogenic controls. Furthermore, expression of LMOD3, which is present at

low levels in cardiomyocytes[15], was unaltered in *LMOD2* W398* hiPSC-CMs, indicating it is unlikely to compensate for the decrease in mutant *LMOD2* levels. Overall, protein analysis revealed *LMOD2* W398* hiPSC-CMs express low levels of truncated LMOD2 protein and have unaltered expression of specific thin and thick filament regulatory proteins.

LMOD2 W398* hiPSC-CMs display loss of LMOD2 pointed-end localization in cardiac thin filaments

Since Lmod2 has vital functions at the level of the sarcomere, the subcellular effects of the *LMOD2* W398* mutation in hiPSC-CMs were next explored. Immunofluorescence microscopy revealed almost undetectable/punctate staining for truncated LMOD2 (using an anti-N-terminus LMOD2 antibody) in W398* hiPSC-CMs, whereas isogenic controls demonstrated LMOD2 at the pointed ends of actin-thin filaments (see Supplemental Fig. 3a, b for line scan analysis of LMOD2 intensity flanking the Z-disc marker, α-actinin). This finding is consistent with our immunoblot analysis demonstrating decreased expression of LMOD2 truncated protein in mutant hiPSC-CMs. Due to the antagonistic relationship between Lmod2 and Tmod1 at the pointed end of cardiac thin filaments[23], TMOD1 localization was also examined to determine if the *LMOD2* W398* mutation affects TMOD1 distribution. Mutant and isogenic hiPSC-CMs both displayed TMOD1 localization at the pointed end of thin filaments (see Supplemental Fig. 3c, d for line scan analysis showing TMOD1 intensity peaks flanking α-actinin). Therefore, the *LMOD2* W398* mutation does not appear to alter the localization of TMOD1 in hiPSC-CMs. To further investigate the subcellular effects of the *LMOD2* W398* mutation, the localization of an additional thin filament binding protein, CAP2[24], and a thick filament protein, myosin, were analyzed (Supplemental Fig. 4). Both isogenic and mutant hiPSC-CMs showed CAP2 and myosin localizing in association with thin and thick filaments, respectively, demonstrating thin and thick filament-associated proteins were not perturbed in *LMOD2* W398* hiPSC-CMs. Overall, subcellular analysis revealed mutant hiPSC-CMs display almost undetectable levels of truncated LMOD2 protein, while isogenic controls demonstrated the expected localization of LMOD2. Furthermore, the *LMOD2* W398* mutation did not affect the distribution of myosin, CAP2, and TMOD1.

Thin filament lengths are significantly shorter in *LMOD2* W398* hiPSC-CMs

Lmod2 is a potent nucleator of actin filaments in vitro, and has a role in the assembly/ maintenance of mature thin filaments in myocytes by promoting thin filament elongation and fine-tuning thin filament lengths[10,23]. To carry out its functions, Lmod2 possesses three actin-binding sites. Although the precise function of all three actin-binding sites is not well understood, the third actin-binding site (comprised of a WH2 domain) has been demonstrated to be important in Lmod2's elongation function[23]. Therefore, to determine the effect of the *LMOD2* W398* mutation (which lacks the third actin-binding site) on Lmod2's ability to regulate thin filaments, thin filament lengths were analyzed. *LMOD2* W398* hiPSC-CMs demonstrated significantly shorter thin filament lengths compared to isogenic controls at sarcomere lengths of 2.0–2.5 μm (0.87 ± 0.09 μm and 0.83 ± 0.10 μm, means ± s.d, $p = 0.0002$, control and mutant hiPSC-CMs, respectively) (Fig. 2). This correlated to a ~ 5% decrease in actin-thin filament lengths in mutant hiPSC-CMs. No statistical difference between sarcomere lengths was detected, indicating thin filament lengths were not shorter due to a decrease in sarcomere length or an artifact of cell fixation. To further validate if the decrease in thin filament lengths was a direct result of the *LMOD2* W398* mutation, mutant hiPSC-CMs were transduced with adenovirus expressing full-length Lmod2 (adv-myc-Lmod2) at a low multiplicity of infection (MOI) of 5. Following the addition of full-length Lmod2, thin filament lengths increased to that of isogenic control levels in mutant hiPSC-CMs (0.83 ± 0.10 μm and 0.86 ± 0.07 μm, means ± s.d, $p = 0.03$, *LMOD2* W398* and W398* hiPSC-CMS with myc-Lmod2, respectively), confirming the *LMOD2* W398* mutation affects thin filament length regulation.

LMOD2 W398* hiPSC-CMs display myofibril misalignment, exhibit altered contractile properties, and perturbed calcium handling dynamics

Dilated cardiomyopathy (DCM) is characterized by impaired systolic performance, interstitial fibrosis, and a contractile deficit of the heart, all of which culminate in dilation of the ventricular chambers, resulting in eventual heart failure. To assess whether *LMOD2* W398* hiPSC-CMs display characteristics common to a DCM-specific phenotype, as observed previously in our *Lmod2*-KO mice[10], the organization of myofibrils in hiPSC-CMs was examined via immunofluorescence microscopy. hiPSC-CMs were probed with fluorescently-conjugated phalloidin, which labels filamentous actin, and an anti-α-actinin antibody, which labels the Z-disc protein, α-actinin. Since α-actinin is an indicator of overall sarcomeric integrity, it was used as a marker to determine potential differences in sarcomeric organization between mutant and isogenic control hiPSC-CMs. At day 30 after differentiation, *LMOD2* W398* hiPSC-CMs displayed a

significant decrease in coherency (a measure of myofibril alignment), indicating *LMOD2* W398* hiPSC-CMs have a disordered sarcomeric pattern (Fig. 1c, d). To determine if this disorganization has a functional consequence, we next examined if *LMOD2* W398* hiPSC-CMs display altered contractile properties, characteristic of DCM. Video optical recordings of electrically paced (1 Hz) hiPSC-CMs were taken and analyzed using the contractile analysis software, MuscleMotion[25]. Compared to isogenic controls, *LMOD2* W398* hiPSC-CMs showed significantly reduced contraction amplitude (~ 21% reduction) (Fig. 3a, b). The duration of contraction, the time to peak (the time at which maximal contraction is achieved), and contraction amplitude were all significantly reduced in *LMOD2* W398* hiPSC-CMs (Fig. 3d, e, f). Conversely, the peak-to-peak time (the average time from one peak of contraction to the next peak of contraction) was unaltered in *LMOD2* W398* hiPSC-CMs (Fig. 3g).

To confirm that the observed changes in contractile parameters of *LMOD2* W398* hiPSC-CMs were a result of the *LMOD2* W398* mutation,
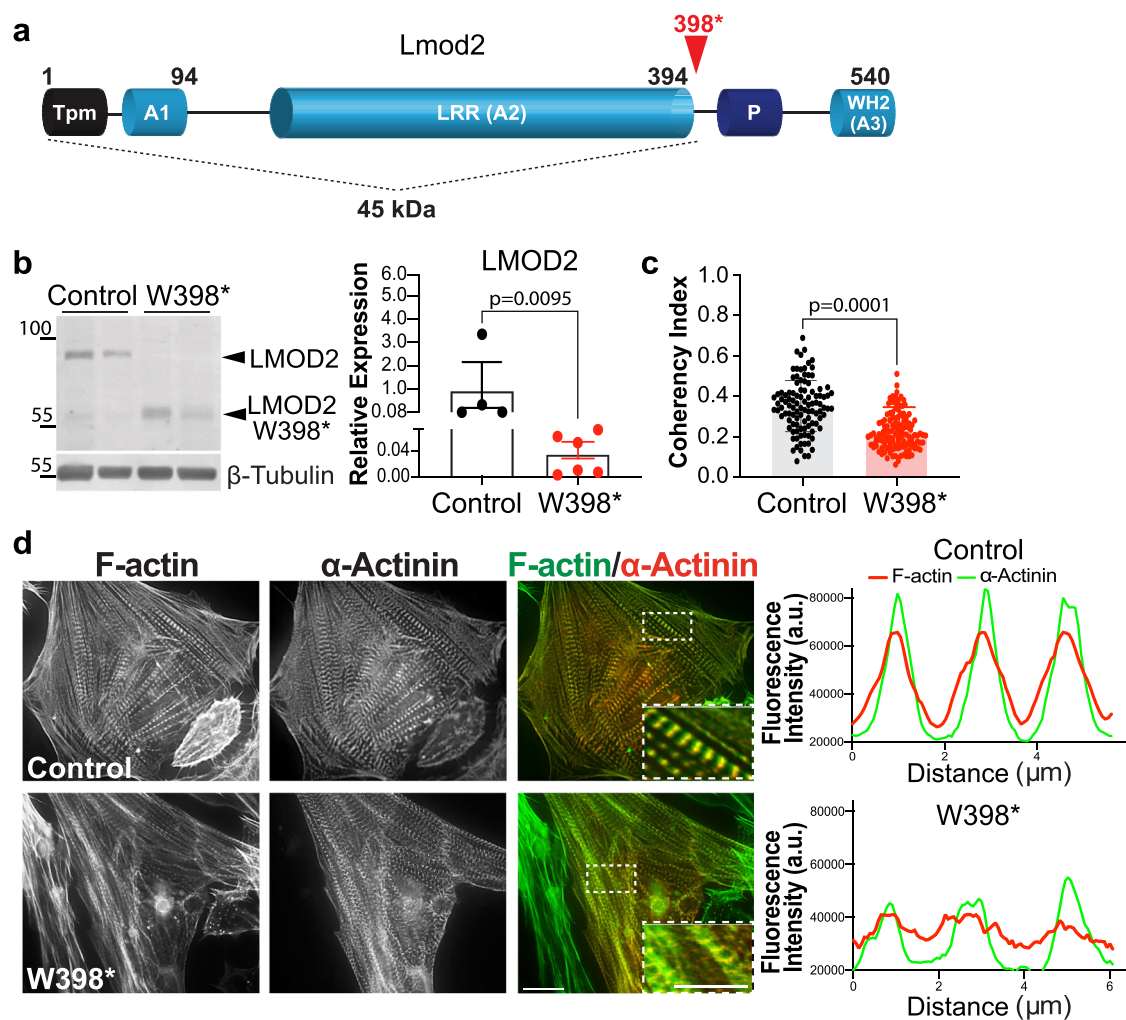

Fig. 1 | Patient-specific *LMOD2* W398* hiPSC-CMs express low levels of truncated LMOD2 protein and display increased sarcomeric misalignment. a Domain structure of Lmod2 (Tpm: tropomyosin binding site, A1: actin-binding site 1, A2: actin-binding site 2 (LRR, leucine-rich repeat), P: proline-rich region, A3: actin-binding site 3 (WH2, Wiskott-Aldrich-Syndrome protein homology 2). The *LMOD2* W398* mutation is predicted to result in a ~ 45 kDa truncated protein. **b** Immunoblot showing full-length LMOD2 expressed in isogenic control hiPSC-CMs and truncated LMOD2 protein expressed in *LMOD2* W398* hiPSC-CMs. Quantification of immunoblots shows significantly decreased expression of truncated LMOD2 in mutant hiPSC-CMs. Relative expression levels were determined following normalization to β-Tubulin. Values are means ± s.e.m., Mann-Whitney

test, two-tailed, *N* = 4–6 independent cardiac differentiations. **c** Quantification of sarcomeric alignment using the anti-α-actinin stain to measure the average coherency index. Control hiPSC-CMs, *n* = 104 cells from 3 individual cardiac differentiations; *LMOD2* W398* hiPSC-CMs, *n* = 131 cells from 4 individual cardiac differentiations, Student's *t*-test, two-tailed, values are means ± s.e.m.
d Representative immunofluorescence images of isogenic control (top) and mutant (bottom) *LMOD2* W398* hiPSC-CMs stained with fluorescently conjugated phalloidin (F-actin) and anti-α-actinin antibodies (Z-disc marker) (scale bar = 2 μm). Line scan analysis showing patterns for F-actin and α-actinin distributions (y-axis, fluorescence intensity in arbitrary units; x-axis, distance in μm).
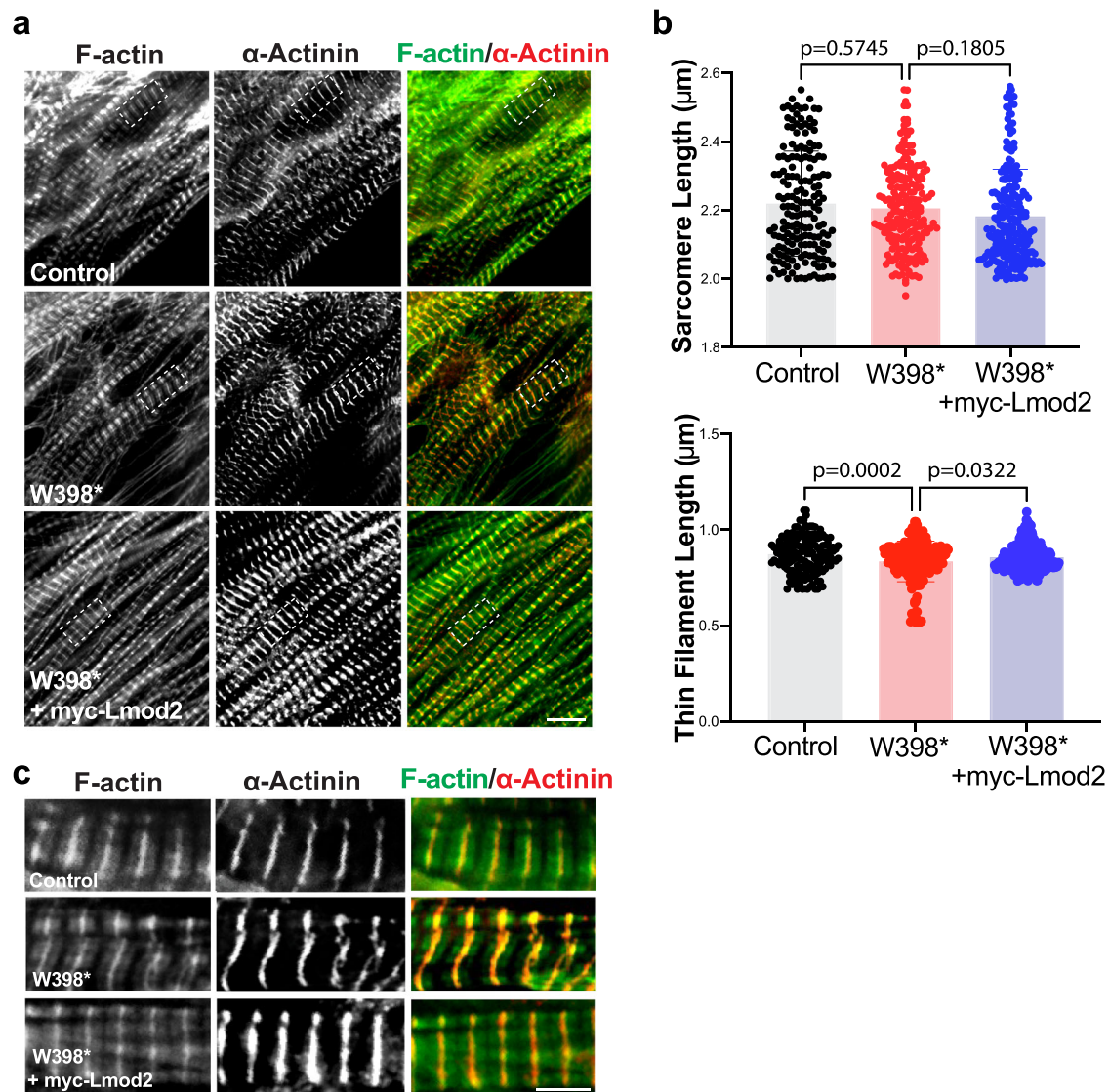
Fig. 2 | *LMOD2* W398* hiPSC-CMs have significantly shorter actin-thin filament lengths. a Representative immunofluorescence images showing α-actinin and fluorescently-conjugated phalloidin in isogenic, *LMOD2* W398* and W398* transduced with myc-Lmod2 hiPSC-CMs. Dashed boxes demonstrate areas of enlarged images in (B). Scale bar = 2 μm. **b** Enlargement of areas marked in (A). Scale bar = 2 μm. **c** Thin filament lengths were significantly shorter in *LMOD2* W398* hiPSC-CMs compared to isogenic controls (0.87 ± 0.095 μm and 0.83 ± 0.105 μm, respectively) and addition of adv-myc-Lmod2 to mutant hiPSC-CMs restored thin filament lengths to near wild-type levels (0.86 ± 0.069 μm and 0.87 ± 0.095 μm, W398* hiPSC-CMS with myc-Lmod2 and isogenic hiPSC-CMs, respectively). Note: thin filament measurements represent half the length of thin filament arrays extending from the Z disc. Values are means ± s.d., *n* = 10–20 cells per cardiac differentiation, 172, 215 and 237 measurements from control, *LMOD2* W398* and *LMOD2* W398*+ myc-Lmod2, respectively, 4-5 independent cardiac differentiations, one-way ANOVA with Tukey's multiple comparisons test.

as opposed to secondary or compensatory effects, adv-myc-Lmod2 was re-introduced into mutant hiPSC-CMs. All previously reported contractile parameters including contraction duration, time to peak, and contraction amplitude were significantly increased in mutant hiPSC-CMs transduced with adenoviral myc-Lmod2 compared to mutant hiPSC-CMs alone (Fig. 3c–f). These results confirm that mutant *LMOD2* W398* hiPSC-CMs have altered contractile properties.

Critical to cardiomyocyte contraction and relaxation is efficient calcium cycling. Having established *LMOD2* W398* hiPSC-CMs exhibit altered contractile properties, we next determined whether mutant hiPSC-CMs have concomitant alterations in calcium handling dynamics. Assessment of calcium transients using the ratiometric dye Fura-2 in electrically paced (1 Hz) hiPSC-CMs revealed *LMOD2* W398* hiPSC-CMs have a significantly reduced Ca^{2+} transient amplitude (~ 37%) (Fig. 3h, i), indicating that the amount of Ca^{2+} available for contraction is greatly reduced in

mutant hiPSC-CMs. This coincides with the reduction in contraction amplitude observed in *LMOD2* W398* hiPSC-CMs, implying an overall decrease in force production. Additionally, there was a reduction in the time to 20% and 80% Ca^{2+} release (Fig. 3j, k) and a reduction in the time for calcium reuptake at 80% but not at 20% reuptake (Fig. 3l, m). The decay tau, an indicator of calcium reuptake into the sarcoplasmic reticulum, was significantly decreased in mutant hiPSC-CMs (~ 42%) (Fig. 3n). Overall, the faster calcium release and reuptake kinetics of *LMOD2* W398* cardiomyocytes provide a potential explanation for the decreased contraction time observed in these cells.

To further examine the relationship between the *LMOD2* W398* mutation and alterations observed in calcium handling, adv-myc-Lmod2 was transduced into mutant hiPSC-CMs. Analysis of calcium transients revealed that adenoviral myc-Lmod2 transduction recovered the transient amplitude in mutant hiPSC-CMs (~ 91% of WT amplitude) (Fig. 3h–n). To

further understand the change in calcium availability, immunoblot analysis of Ca^{2+} handling proteins was performed and showed no detectable change in expression of L-type Ca^{2+} channel, sodium-calcium exchanger (NCX), SERCA2a, calsequestrin-2 (CASQ2), and phospholamban (PLN) in *LMOD2* W398* hiPSC-CMs (Supplemental Fig. 5). This suggests that expression of the latter Ca^{2+} handling proteins were unaltered in mutant hiPSC-CMs and that calcium dysregulation is occurring elsewhere in the calcium-contraction signaling pathway.

LMOD2 W398* hiPSC-CM engineered heart tissues have decreased force production

Since *LMOD2* W398* hiPSC-CMs displayed altered contractile and calcium handling dynamics in 2D cultures (i.e., a monolayer of hiPSC-CMs), we sought to determine if these properties translate to the tissue level. Engineered heart tissues (EHTs) provide a unique opportunity to study the contractile kinetics of hiPSC-CMs under conditions that more closely mimic the native heart. Scaffolding polymers are combined with hiPSC-CMs to create cardiac muscle tissue constructs that generate contractile force, exhibit electrical coupling and cellular organization, whereby polydimethylsiloxane (PDMS) posts bend proportionally to the amount of force generated (for review[26]) (Fig. 3o). The deflection that occurs can be quantified through video optical recordings. On day 10 after differentiation, control and *LMOD2* W398* hiPSC-CM EHT constructs were generated. Within 3-5 days, EHTs began to beat and were electrically paced starting at 0.6 Hz. Electrical pacing was gradually increased to 2.0 Hz over the course of 20 days, using frequency-ramped electrical pacing to avoid toxic electrolysis. Over the duration of the experiment, *LMOD2* W398* EHTs demonstrated a decrease in force production, specifically at higher frequencies (~ 65% force reduction at 2.0 Hz) when compared to isogenic control EHTs (Fig. 3p). In addition, mutant EHTs demonstrated a decrease in contraction time (212.9 ± 105.2 ms vs 45.0 ± 52.6 ms, control vs LMOD2 W398* hiPSC-CMs at 2.0 Hz, respectively) (Fig. 3q). Interestingly, two out of 6 mutant EHT constructs stopped beating when pacing was increased to 1 Hz. Overall, EHT analysis demonstrated a decrease in force production and a decrease in contraction time, similar to our reported findings in monolayer hiPSC-CM cultures.

Lmod2 W405* homozygous mice present with dilated cardiomyopathy which is prevented via introduction of wild-type GFP-Lmod2

In addition to examining the effects of the *LMOD2* W398* mutation in hiPSC-CMs, a mouse model harbouring the homologous mutation, *Lmod2* p.W405*, was generated using CRISPR/Cas knock-in technology and studied in parallel to determine the in vivo effects of the Lmod2 mutation. To analyze in vivo cardiac function of these mice, transthoracic M-mode echocardiography was performed at various time points (postnatal day 21 (P21), when the majority of *Lmod2*-null mice died after rapidly developing DCM[9]; P70, early adulthood; and P180, mature adulthood). Mice homozygous for the *Lmod2* p.W405* mutation (henceforth referred to as *Lmod2* W405* mice) have significantly larger left ventricle (LV) internal diameters in diastole and systole compared to wild-type mice at all time points measured (Fig. 4a and Supplemental Fig. 6a). They also have thinner LV walls, most evident at P180 (Fig. 4a and Supplemental Fig. 6a). Accordingly, the eccentricity index, the ratio of chamber diameter to combined anterior and posterior wall thicknesses in diastole, is also increased, indicating eccentric remodeling (Fig. 4a). Furthermore, LV ejection fraction (EF) is significantly reduced at all three time points (Fig. 4a). Taken together, these morphological and functional alterations are consistent with dilated cardiomyopathy.

The *Lmod2* W405* mice begin to die at ~6 months of age with a median survival of 186 days (Fig. 4b). Immunoblot analysis of LV tissue at P70 showed that mutant mice express truncated Lmod2 protein at approximately 45% of wild-type (full-length) Lmod2 levels (Fig. 4c). Interestingly, neonatal cardiomyocytes isolated from *Lmod2* W405* mice at ~P3 and cultured for four days display a larger reduction in mutant Lmod2

protein levels, with only around 10% of wild-type Lmod2 levels. We next analyzed cardiac thin filament lengths in the mutant mice. It has been previously shown that thin filament length varies with sarcomere length; although the mechanism underlying this observation is unknown[27,28]. Therefore, to ensure any observed differences in thin filament length are independent of sarcomere length changes, we: 1) plotted thin filament length vs sarcomere length for each animal, 2) fit the data with a simple linear regression curve, 3) used the curve to determine thin filament length at a defined sarcomere length (2.2 μm) and 4) averaged the thin filament lengths of wild-type and *Lmod2* W405* mice. Thin filament lengths were reduced at both P21 (0.74 ± 0.02 μm vs 0.84 ± 0.02 μm) and P70 (0.78 ± 0.03 μm vs 0.86 ± 0.03 μm) in the LVs of *Lmod2* W405* compared to wild-type mice, respectively (Fig. 4d).

The echocardiography results suggest that cardiac contractility is impaired in the *Lmod2* W405* mice. Therefore, the organization of myofibrils in *Lmod2* W405* LV tissue was next examined via immunofluorescence microscopy to assess sarcomeric organization. Similar to our findings in mutant hiPSC-CMs (Fig. 1c), *Lmod2* W405* mice displayed a significant decrease in coherency, indicating increased myofibril misalignment (Supplemental Fig. 6b, c). To further analyze contractility at the cellular level, tension generated by demembranated interventricular septal cells was measured in response to varying levels of Ca^{2+}. Maximum calcium-activated tension was significantly reduced (16.8 ± 2.0 mN/mm^2 vs 30.8 ± 2.6 mN/mm^2), while the sensitivity of the myofilament to calcium was increased ($EC_{50} = 2.50 \pm 0.12$ μM vs 2.74 ± 0.20 μM) in *Lmod2* W405* vs wild-type cardiomyocytes, respectively (Fig. 4e). Alterations in cellular contraction and calcium handling were further corroborated in electrically paced (1 Hz) neonatal cardiomyocytes isolated from *Lmod2* W405* mice. Analysis revealed a significant decrease in contraction amplitude (~ 32%) and a significantly reduced Ca^{2+} transient amplitude (~ 37%) (Supplemental Fig. 7a–m). This indicates that the amount of Ca^{2+} available for contraction is greatly reduced in *Lmod2* W405* mice, similar to mutant hiPSC-CMs. To further understand the dysregulation in calcium dynamics, immunoblot analysis was performed for various Ca^{2+} handling proteins in *Lmod2* W405* left ventricular tissue (Supplemental Fig. 7n–v). At day 20 a significant increase in CASQ2 expression was detected, however, at day 70 no significant difference in Ca^{2+} regulatory protein expression was observed. Thus, it may be that dysregulation of calcium dynamics is caused by other regulatory elements within the calcium signaling cascade, such as phosphorylation of phospholamban, ryanodine receptor-2 (RyR2), or PKA receptors. To examine this further, immunoblot analysis was performed on PLN, RyR2, and PKA phosphorylation sites in day 70 *Lmod2* W405* left ventricular tissue (Supplemental Fig. 8a–h). However, no statistical difference was detected in the relative expression of RyR2 (pSer[2808] or pSer[2814]), PLN (pSer[16] or pThr[17]), or PKA (RIIα or RIIβ) phosphorylation sites, indicating other mechanisms underlie the alteration of calcium handling in the *Lmod2* W405* mice.

To determine if full-length, wild-type Lmod2 is functional in the presence of Lmod2 W405* mutant protein, and able to prevent onset of disease, we injected adeno-associated virus (AAV2/9) expressing GFP-tagged wild-type Lmod2 into the pericardial space of *Lmod2* W405* mice at P4. Echocardiography at P21 revealed that cardiac dilation and reduction of systolic performance evident in *Lmod2* W405* mice was ameliorated by expression of GFP-Lmod2 (Fig. 5a and Supplemental Fig. 6d). Immunoblot analysis showed that Lmod2 W405* mutant protein is expressed at ~45% of endogenous wild-type Lmod2 levels following expression of GFP alone (Fig. 5b), which is consistent with the reduction observed at P70 (Fig. 4b). Although variable, GFP-Lmod2 expression in *Lmod2* W405* mice averaged ~50% of wild-type Lmod2 levels (Fig. 5b). Interestingly, Lmod2 mutant protein levels decreased even more following expression of GFP-Lmod2 to ~20% of endogenous wild-type Lmod2 protein levels.
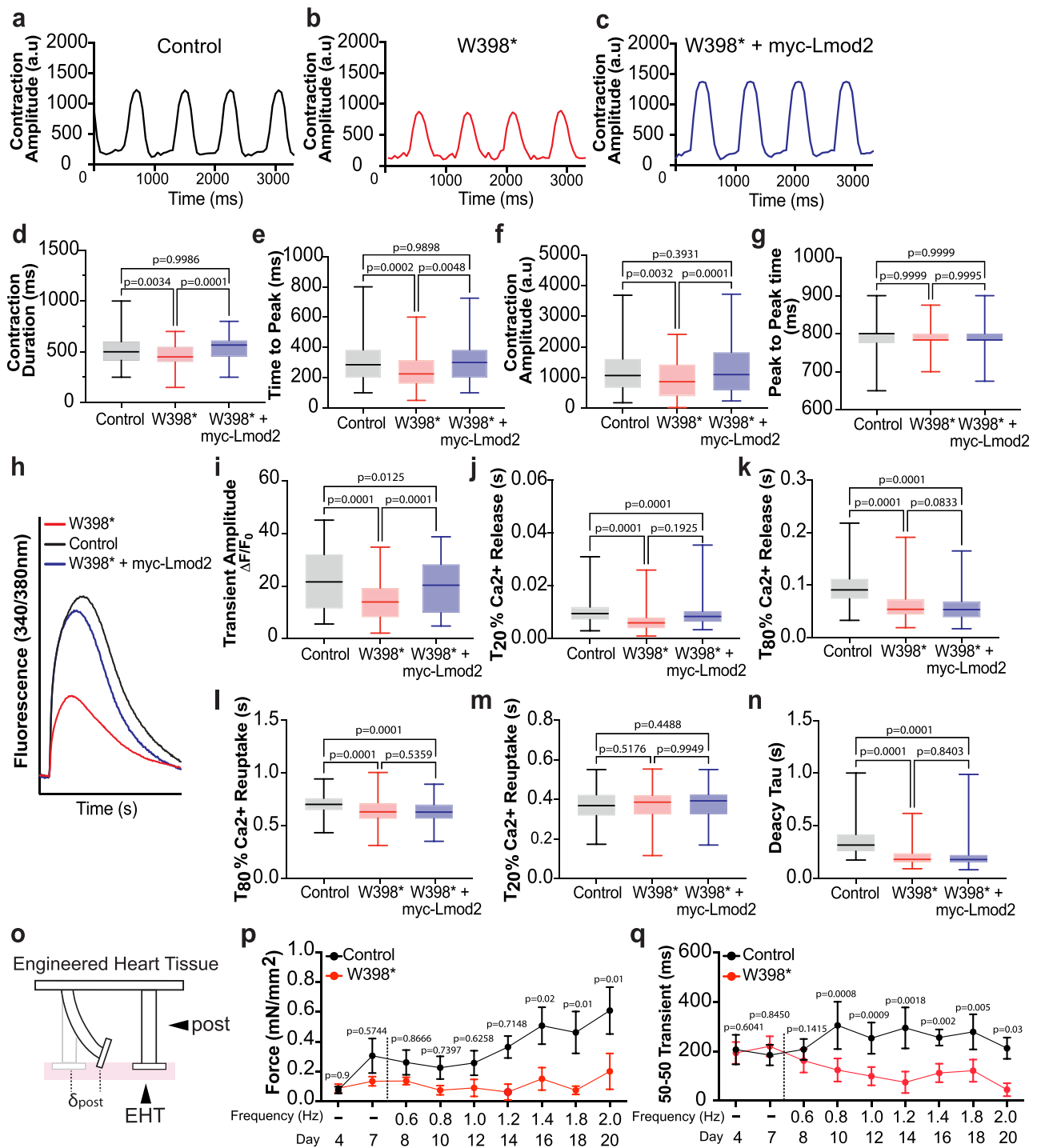
Fig. 3 | *LMOD2* W398* hiPSC-CMs exhibit altered contractile properties, calcium handling dynamics, and force production. Representative contractility traces of control (**a**), *LMOD2* W398* (**b**) and *LMOD2* W398*+myc-Lmod2 (**c**) electrically paced (1 Hz) hiPSC-CMs. **d**–**g** Contractile parameters; duration of contraction (ms), time to peak (ms), contraction amplitude (a.u.), and peak to peak time (ms), respectively. n = 115-202 measurements in hiPSC-CMs, N = 3-4 independent cardiac differentiations, one-way ANOVA with Tukey's multiple comparisons test. **h** Representative calcium transients in electrically paced (1 Hz) hiPSC-CMs. **i**–**n** Calcium transient measurements at 1 Hz pacing comparing the transient amplitude, time to 20% (T_{20}) and 50% (T_{50}) of Ca^{2+} release, time to 80% (T_{80}) and 50% (T_{50}) Ca^{2+} reuptake and decay tau in control, *LMOD2* W398*, and *LMOD2* W398* + myc-Lmod2 hiPSC-CMs. n = 205-258 measurements in hiPSC-CMs, N = 3-4 independent cardiac differentiations, one-way ANOVA with Tukey's

multiple comparisons test. **o** Graphical representation of an engineered heart tissue (EHT). Scaffolding polymers were combined with hiPSC-CMs and seeded within an agarose mold containing polydimethylsiloxane (PDMS) posts. The contractile force generated by EHT constructs was proportionally measured by the deflection of PDMS posts and quantified through video optical recordings. **p** Force production normalized to cross-sectional area in control and *LMOD2* W398* hiPSC-CM EHTs over time with increasing pacing frequency. **q** Contraction time (50-50 transient) of *LMOD2* W398* hiPSC-CM and isogenic control EHTs. Grey dashed line indicates the start of pacing in EHTs. n = 6 EHT constructs from N = 3 independent differentiations, mixed effects analysis with Sidak's multiple comparisons test. D4 = day 4 prior to pacing, D7 = day 7 prior to pacing. All values are means ± s.e.m. Box and whisker plots show median (horizontal line), standard deviation (box) and maximum and minimum values (whiskers), ms milliseconds; a.u arbitrary units.
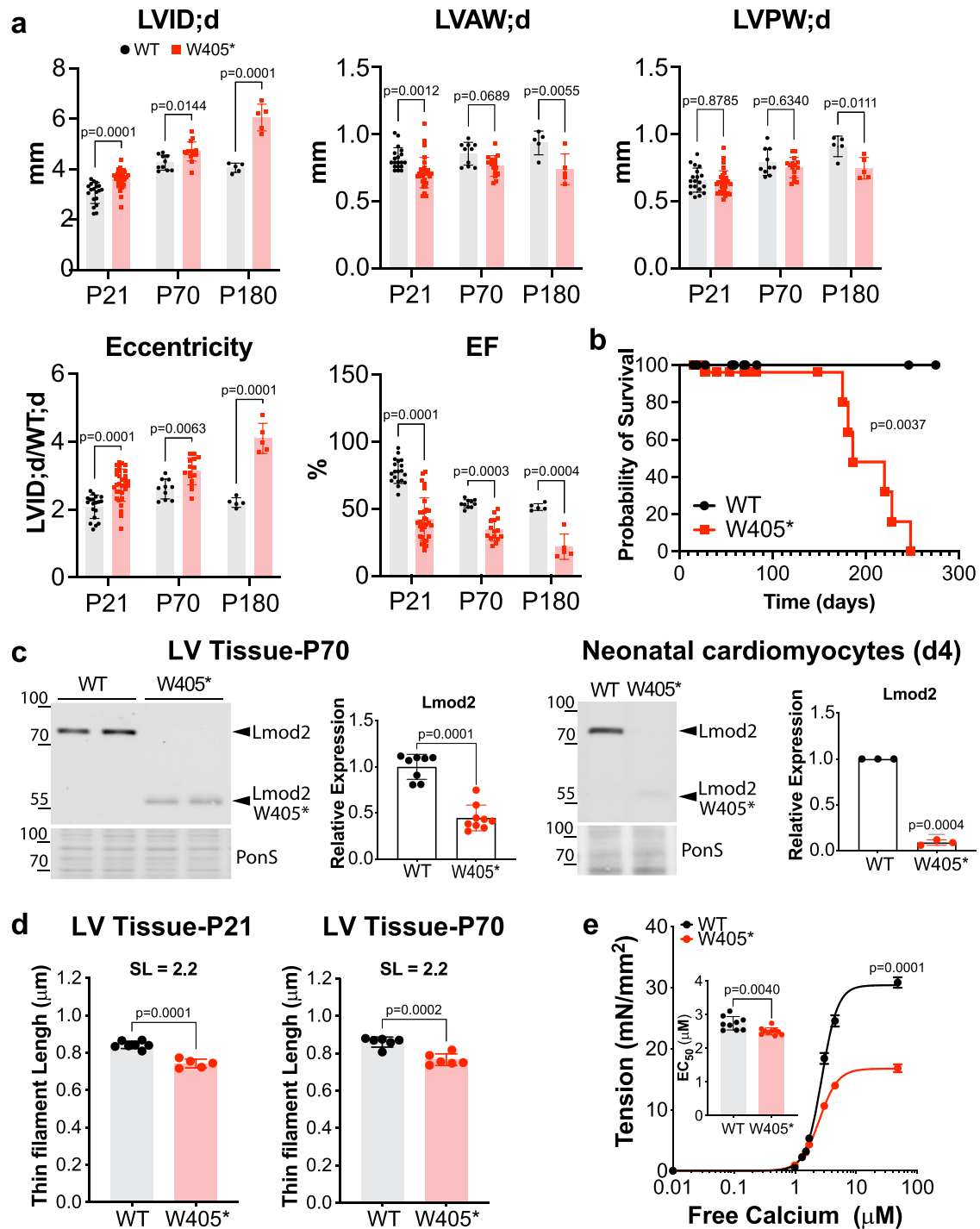
Fig. 4 | *Lmod2* W405* mice display dilated hearts with shorter thin filaments and reduced contractility. a Echocardiography of wild-type (black) and *Lmod2* W405* (red) mice at postnatal days 21, 70 and 180. LVID;d, left ventricle internal diameter in diastole; LVAW;d, left ventricle anterior wall thickness in diastole, LVPW;d, left ventricle posterior wall thickness in diastole, Eccentricity (left ventricle internal diameter in diastole / combined anterior and posterior wall thicknesses in diastole); EF, ejection fraction. n = 19–31 (P21), 10–15 (P70), and 5 (P180), one-way ANOVA with Sidak's multiple comparison test. **b** Percent survival of wild-type (black) and *Lmod2* W405* (red) mice over time. **P < 0.01, log-rank (Mantel-Cox) test. **c** Immunoblot analysis of LV lysate from P70 mice (left two panels) or cell lysate from day 4 neonatal cardiomyocytes in culture (right two panels) probed with an antibody to Lmod2. Relative expression levels were determined following normalization to total protein levels assessed via Ponceau S staining. n = 8-9 (P70) and 3 (neonatal cardiomyocyte cultures), Student's *t*-test, two-tailed (P70), One sample t-test (neonatal cardiomyocyte cultures). **d** Mean thin filament length at a sarcomere length of 2.2 μM. n = 5–7 (P21) and 6 (P70), Student's *t*-test, two-tailed. **e** Active tension generated at various concentrations of free Ca^{2+} is plotted for single cardiomyocytes isolated from wild-type (black) and *Lmod2* W405* (red) mice. The inset represents the mean EC_{50} of calcium activation. n = 9-10 animals, 4-5 cells/animal, Student's *t*-test, two-tailed. All values are means ± s.d.

Fig. 5 | Introduction of wild-type (full length) GFP-Lmod2 reduces the development of cardiac disease in *Lmod2* W405* mice.
a Echocardiography of wild-type mice expressing GFP (black), *Lmod2* W405* mice expressing GFP (red) and *Lmod2* W405* mice expressing GFP-Lmod2 (blue) at postnatal day 21. LVID;d, left ventricle internal diameter in diastole; LVAW;d, left ventricle anterior wall thickness in diastole, LVPW;d, left ventricle posterior wall thickness in diastole, Eccentricity (left ventricle internal diameter in diastole / combined anterior and posterior wall thicknesses in diastole); EF ejection fraction. $n = 6$, one-way ANOVA with Tukey's multiple comparison test. **b** Immunoblot analysis of LV lysate from mice collected at P28 and probed with antibodies to Lmod2 and GFP. Relative expression levels were determined following normalization to total protein levels assessed via Ponceau S staining. $n = 6$, one-way ANOVA with Tukey's multiple comparison test. All values are means ± s.d.
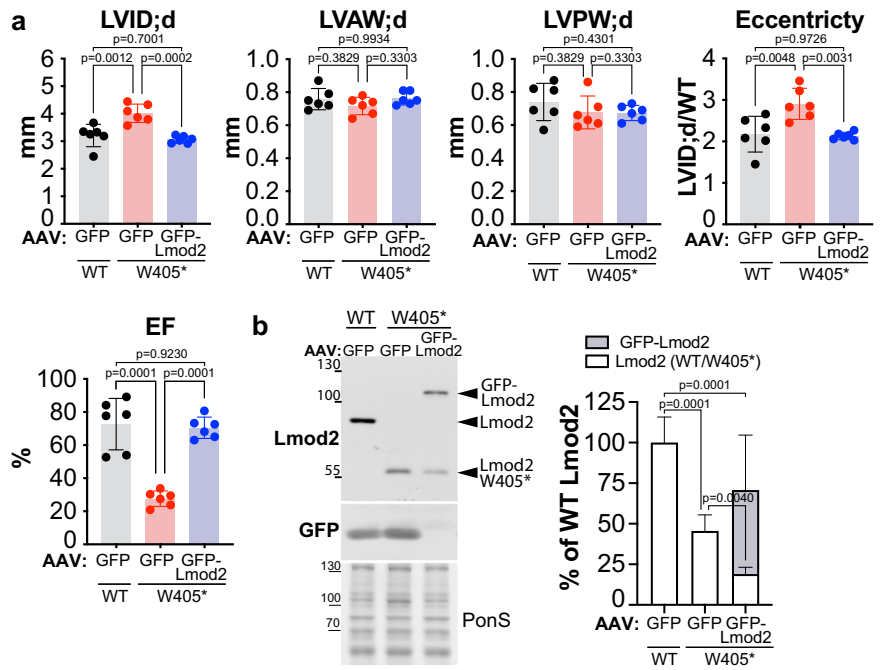
Lmod2 W405* homozygous mice and *Lmod2*-KO mice display significant changes in actin and transcription factor-related genes

Since *Lmod2* W405* homozygous mice display evidence of morphological and functional changes consistent with DCM, we examined differences in the transcriptomes of mutant mice to decipher underlying signaling mechanisms of this disease process. To elucidate a common pathway for Lmod2-associated DCMs *Lmod2*-KO mice were also subject to transcriptome analysis. Bulk RNA-sequencing of LV free wall tissue was performed at P4, prior to *Lmod2*-null mice demonstrating ventricular dilation[9]; and P14, when *Lmod2*-null mice display ventricular dilation but preceding death at P20. We identified 15 differentially expressed genes (DEGs) (padj < 0.05) in *Lmod2* W405* and 226 DEGs (padj < 0.05) in *Lmod2*-KO mice at P4, with *Lmod2* significantly downregulated in both mouse models (padj 7.14e-38 and padj 2.57e-246, respectively). At P14, 1073 DEGs (padj < 0.05) in *Lmod2* W405* and 856 DEGs (padj < 0.005) in *Lmod2*-KO mice were identified (Fig. 6a), with 400 DEGs common to both mouse models (Fig. 6b). Next, overlapping genes were subject to Motif Enrichment Analysis (Fig. 6c). Upregulated DEGs were found to have enrichment in binding motifs associated with cardiogenesis and cardiac remodeling (*Mef2d, Mef2c* and *Jun-AP1*) while *Lhx3* and *Klf14* were identified to control transcription of downregulated genes. Gene set enrichment analysis (GSEA) was used to acquire transcription factor (TF), human phenotype (HP), and biological processes (BP) enrichment terms between overlapping genes and identified upregulated (*Mef2, Pitx2, Ap1*) and downregulated (*Srf, Nfkb*) TF genes as well as upregulated pathways associated with DCM and abnormal muscle fiber morphology (Fig. 6d). BP enrichment terms identified upregulation of ion transport and downregulation of cell cycle processes (Supplemental Fig. 9a). When DEGs were mapped in STRING (Search Tool for the Retrieval of Interacting Genes/Proteins), network analysis identified enrichment of protein-protein interactions related to *Lmod2* including *Acta2, Pdlim1, Mypn* and *Fhl2* (Fig. 6e). Lastly, when gene expression was examined at P4 and P14 between *Lmod2* W405* and *Lmod2*-KO mice significant changes were observed at P14 in actin-related genes, notably *Acta2, Actn2, Lmod2, Mypn*, and *Pdlim1*, which are all implicated in cardiac sarcomere architecture and function (Fig. 6f). Interestingly, a subset of these genes revealed an upregulation of *Fhl2*, a gene that encodes a cardiac-specific LIM protein, as well as Z-disc and intercalated disc genes (e.g., *Tcap, Nrap*, and *Flnc*). Immunoblot analysis verified increased expression of NRAP and

Filamin-C in P20 *Lmod2* W405* and *Lmod2*-KO mouse LV tissue (Supplemental Fig. 8i–l), however, a significant increase in the expression of FHL2 was only detected in *Lmod2*-KO mouse tissue (Supplemental Fig. 8m–p).

LMOD2 W398* hiPSC-CMs have significant changes in transcriptomic signatures related to myofilament, transcription factor, and calcium-regulatory genes

To further characterize and delineate the differences in the transcriptomic signatures of mutant and control hiPSC-CMs, bulk RNA-sequencing was performed and identified 530 DEGs (padj < 0.005) (Fig. 7a). GSEA analysis of transcription factor (TF), human phenotype (HP), and biological processes (BP) enrichment terms demonstrated downregulation of DEGs associated with several transcription factor-dependent pathways (*SRF, NKX*) and downregulation of pathways associated with calcium and MAPK signaling (Fig. 7b). Additionally, BP enrichment terms demonstrated an upregulation of cellular respiration pathways and a downregulation of neuronal development (Supplemental Fig. 9b). When DEGs were subject to STRING network analysis for retrieval of interacting genes, significant enrichment of protein-protein interactions related to actin regulation (*ACTA2, ACTN1, MYLK* and *FLNA*) and calcium dynamics (*ATP1B1, CAMK4*, and *PLCB3*) were identified. Motif Enrichment Analysis of DEGs displayed upregulated genes have an enrichment in TCF while downregulated genes have an enrichment in MEF2 binding motifs involved in cardiac development and homeostasis (Fig. 7d). Further analysis of gene expression profiles between control and *LMOD2* W398* hiPSC-CMS identified significant differences between actin-related genes such as *ACTA2, ACTB, ACTN1, FHL2, FLNA, MYO1D*, and *PDLIM1*- all associated with cardiac disease pathology and altered cardiac function (Fig. 7e).

LMOD2 regulates SRF activity in an actin-dependent manner

Of the transcriptionally downregulated pathways, the serum response factor (SRF) pathway was identified in both mutant hiPSC-CMs and mouse heart tissue RNA sequencing analysis. Likewise, specific SRF-related genes were discovered to be downregulated in *Lmod2* W405* and *Lmod2*-KO overlapping genes (*Junb, Fos, Acta2*, and *Vcl*) as well as in *LMOD2* W398* hiPSC-CMs (*ACTA2, ACTB, ACTA2, FHL1, TLN1, FLNA, CAP1* and *ACTN1*) (Fig. 8a, b). SRF is a ubiquitously expressed transcription factor, encoded by a single gene that is responsible for activating many downstream
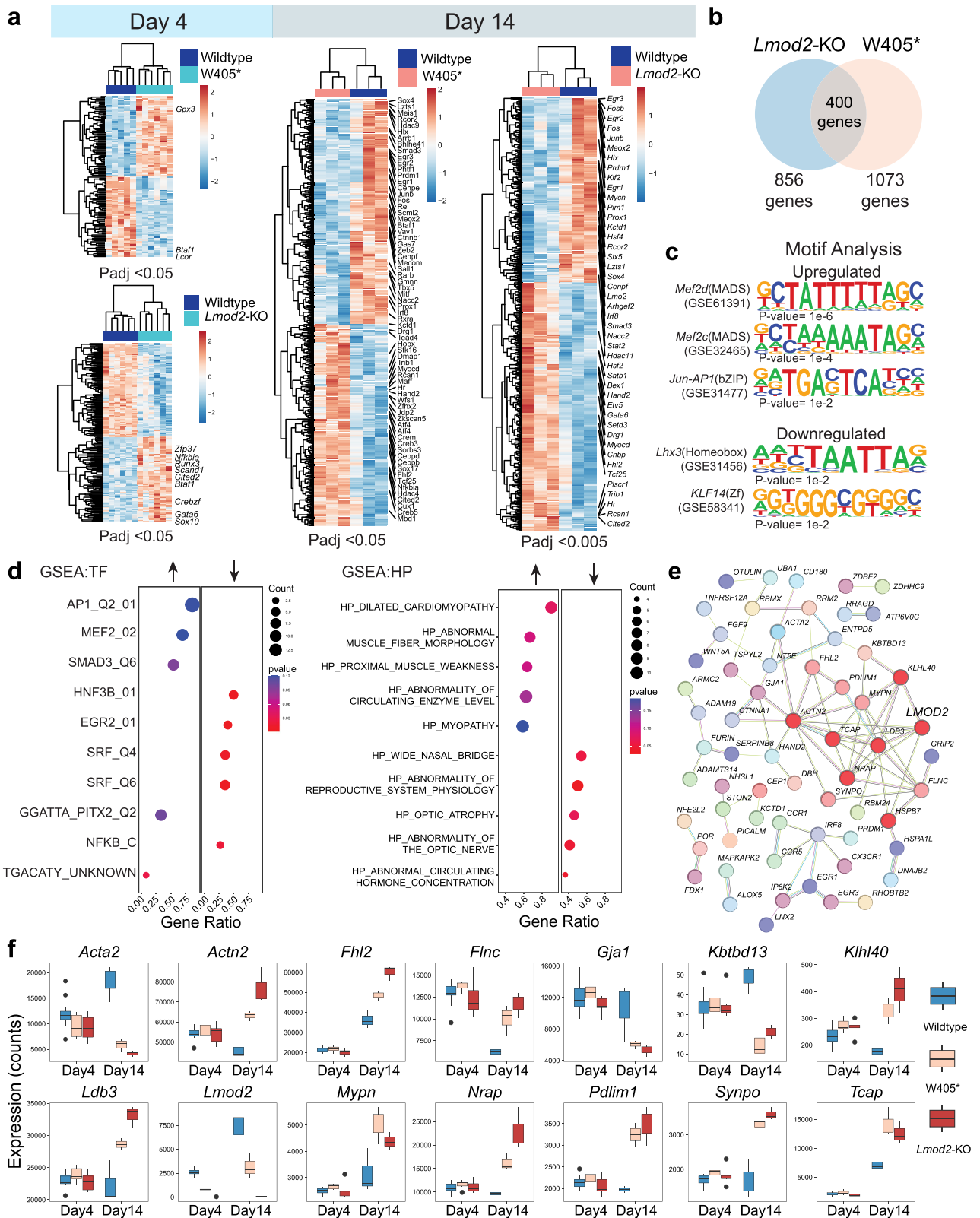
target genes[29,30] involved in cardiovascular development (for reviews[21,31]). Precise regulation of SRF is achieved by activation of many SRF-dependent cofactors such as the ternary complex factor (TCF)[32–35] and myocardin-related transcription factor (MRTF)[36–38]. Activation of the aforementioned SRF-dependent target genes is regulated by MRTF, a G-actin-associated SRF co-activator that translocates from the cytoplasm into the nucleus in response to actin polymerization[39]. Since Lmod2 has a canonical role in regulating actin-thin filament assembly it is possible that perturbation of actin polymerization via the *LMOD2* W398* mutation results in increased monomeric G (globular)-actin which in turn, binds to MRTF, preventing MRTF translocation into the nucleus and activation of SRF-dependent target genes involved in actin dynamics. To test this hypothesis, we first

Fig. 6 | Bulk RNA sequencing of LV tissue from *Lmod2* W405* and *Lmod2*-KO mice demonstrates significant differences in myofilament and transcription factor-related gene signatures. a Heatmap analysis generated from bulk RNA-seq showing differentially expressed genes (DEGs) in *Lmod2* W405* and *Lmod2*-KO versus wild-type mouse left ventricular tissue at days 4 and 14. Transcription factor-related genes are annotated. *n* = 6 (P4) and *n* = 3 (P14). **b** Weighted Venn diagram displaying overlap of 400 DEGs between P14 *Lmod2* W405* and *Lmod2*-KO mice left ventricular tissue. **c** Motif Enrichment Analysis (MEA) for upregulated and downregulated genes derived from overlapping DEGs between *Lmod2* W405* and *Lmod2*-KO mice left ventricular tissue in (B). **d** Gene set enrichment analysis

(GSEA) demonstrating significant upregulated and downregulated transcription factor (TF) and human phenotype (HP)-related genes identified in the overlapping genes between *Lmod2* W405* and *Lmod2*-KO mice left ventricular tissue. *n* = 6 (P4) and *n* = 3 (P14). **e** STRING network analysis of DEGs showing protein-protein interactors with *Lmod2* (red). **f** Gene expression profiles of significant actin regulatory genes identified between *Lmod2* W405*, *Lmod2*-KO mice and wild-type left ventricular tissue. *n* = 6 (P4), padj < 0.05; *n* = 3 (P14), padj < 0.005. Box and whisker plots show median (horizontal line), standard deviation (box) and maximum and minimum values (whiskers).

examined whether the expression of MRTF-SRF-regulated downstream targets were altered. Immunoblot analysis demonstrated decreased expression of α-SMA, CAP1, and FHL1 in mutant mouse LV tissue and/or mutant hiPSC-CMs (Fig. 8c–g). Next, to interrogate whether G-actin levels are increased, LV tissue from *Lmod2* W405* mice was fractionated into F-actin and G-actin by ultracentrifugation. Quantification of immunoblots revealed a significant increase in G-actin (10.6% ± 3.3) compared to wild-type (2.5% ± 0.4) (Fig. 8h). A further increase in G-actin was demonstrated in *Lmod2*-KO LV tissue (11.9% ± 2.3 G-actin vs 3.2% ± 1.1 in wild-type mice) (Fig. 8i). Myosin and/or SERCA2a were used as internal controls to confirm the validity of our fractionation assay. As expected, myosin fractionated with F-actin and SERCA2a with G-actin (Fig. 8h, i).

To examine the cellular localization of MRTFA and MRTFB (two isoforms of MRTF), immunocytochemistry was performed on mutant and isogenic hiPSC-CMs and demonstrated significantly reduced MRTFB nuclear localization (~ 25%) in *LMOD2* W398* hiPSC-CMs (Fig. 8j). In contrast nuclear localization of MRTFA was not statistically different (Fig. 8k). To confirm the total expression of MRTFA and MRTFB was unchanged in hiPSC-CMs and thus not affecting the percentage of nuclear to cytoplasmic localization, immunoblot analysis of whole cell lysate was performed. As expected, mutant hiPSC-CMs did not show a statistically significant difference in the total amount of MRTFB (Fig. 8l) or MRTFA expression (Fig. 8m). To interrogate whether MRTFA and/or MRTFB localization was also altered in the *Lmod2* W405* mice, immunocytochemistry was performed on isolated neonatal cardiomyocytes. Both wild-type and *Lmod2* W405* isolated cardiomyocytes displayed nuclear and cytoplasmic localization of MRTFA and MRTFB, however staining for MRTFB appeared perinuclear, extending to the area surrounding the nucleus (Fig. 9a, c). This was confirmed by quantifying the perinuclear area of both MRTFA and MRTFB, where a significant increase in MRTFB perinuclear area (37.2 ± 7.2a.u vs 130.6 ± 21.6a.u, mean ± s.d., *p* < 0.0001, wild-type vs *Lmod2* W405*, respectively) (Fig. 9b), but not MRTFA (Fig. 9d), was found, suggesting a possible alteration in MRTFB localization. Immunoblot analysis of LV whole cell lysate confirmed the total amount of MRTFA and MRTFB was unaltered at both D20 and D70 (Fig. 9e–g). To further examine localization patterns of MRTFA/B more precisely, fractionation experiments were performed on LV heart tissue from *Lmod2* mutant mice, as described above. When MRTFA and MRTFB expression was examined, MRTFB (6.6% ± 5.3 vs 16.7% ± 4.8, wild-type vs *Lmod2* W405* mice, respectively), but not MRTFA (15.4% ± 8.3% vs 16.1% ± 7.4 wild-type vs *Lmod2* W405* mice, respectively), was found to fractionate with G-actin in *Lmod2* W405* LV tissue (Fig. 9h, i). Similarly, MRTFB (Fig. 9j) (3.7% ± 2.3 vs 17.5% ± 8.9, wild-type vs *Lmod2*-KO mice, respectively), but not MRTFA (Fig. 9k) (4.8% ± 4.3 vs 4.3% ± 2.8, wild-type vs *Lmod2*-KO mice, respectively), was observed to fractionate with G-actin in *Lmod2*-KO LV tissue. These findings suggest a significant proportion of MRTFB is associated with the G-actin pool and is therefore unavailable to activate SRF (and subsequent downstream target genes) in the nucleus of *Lmod2* mutant mice.

Discussion
The use of iPSC-derived cardiomyocytes to study heart disease offers a powerful tool to examine the phenotypic effects of a human mutation with the underlying principle that the pathophysiology of the mutation is

intrinsic to the cardiomyocyte (e.g., cell autonomous), such as mutations arising in sarcomeric proteins[40]. Therefore, to assess the primary effects of the *LMOD2* W398* mutation, hiPSC-CMs and isogenic controls were generated. To assess the in vivo effects, *Lmod2* W405* mice harbouring the homologous mutation were used. Subcellular analysis of mutant hiPSC-CMs showed loss of truncated LMOD2 protein (lacking the C-terminal region containing its third actin-binding site) localization near the pointed ends of cardiac thin filaments, without perturbed localization of two other pointed-end binding proteins, CAP2 and TMOD1. This was corroborated by evidence demonstrating that the expression of mutant LMOD2 was reduced. Similarly, truncated Lmod2 protein was detected in W405* mouse tissue, albeit at ~50% of wild-type levels. It has previously been demonstrated that a strong interaction occurs between actin and the second and third actin-binding domains of Lmod2 (LRR and WH2 domains, respectively) whereas a weaker interaction exists between the N-terminal region of Lmod2 (actin-binding site one) and actin[41]. Additionally, loss of the third actin-binding site leads to weaker actin-nucleation in vitro[42] and is necessary for thin filament elongation[23] (for review[43]). Therefore, the third actin-binding site appears to be important for Lmod2's function. Accordingly, our studies confirmed that loss of the third actin-binding site results in significantly reduced thin filament lengths, both in mutant hiPSC-CMs (~ 5%) and W405* mouse heart tissue (~ 12%) at P21, suggesting Lmod2's ability to polymerize and maintain actin filament lengths is altered. We predict that since the *LMOD2* W398* mutation retains both the first and second actin-binding sites (with the second actin-binding site harboring strong Lmod2-mediated actin polymerization activity[41]), this may have prevented a further decline of thin filament lengths to that observed in *Lmod2*-KO mice (~ 15%)[9]. Alternatively, the dysregulation of thin filament lengths may be due to overall low levels of truncated Lmod2 protein in W398* hiPSC-CMs and W405* mice, preventing Lmod2 from carrying out its native function in the heart. The decrease in truncated protein may also be attributable to proteasomal degradation or a decrease in the levels of its transcript. Since the W398* mutation results in a premature termination codon (PTC), we predict that Lmod2 mutant protein is reduced due to nonsense-mediated mRNA decay (NMD)- a surveillance system that detects mRNA containing PTCs and activates degradation of the transcript (for review[44]). This is supported by our previous results from the patient's explanted heart tissue and in human *LMOD2* gene constructs demonstrating a decrease in Lmod2 mature mRNA but not pre-mRNA levels, implying mutant mRNA is eliminated by NMD.[20,45]

We discovered structural changes in mutant *LMOD2* hiPSC-CMs at the level of the sarcomere, as well as altered contractile properties and compromised ability to regulate calcium flux. In parallel, the *Lmod2* W405* mice demonstrated significantly reduced force production in isolated cardiomyocytes, reduced contractility, and altered calcium handling capabilities. Furthermore, the re-introduction of full-length Lmod2 into W398* hiPSC-CMs resulted in a return of contractile production and calcium regulation to that of control levels, suggesting Lmod2 may have a role in cardiomyocyte contractility. It has previously been predicted that when thin filament lengths are shortened (due to loss of Lmod2) the functional overlap of thick and thin filaments is reduced, therefore fewer myosin heads interact with actin-binding sites, resulting in decreased force produced by each actomyosin interaction[28]. Several different explanations could offer insight into Lmod2's function in cardiomyocyte contraction. At the level of the
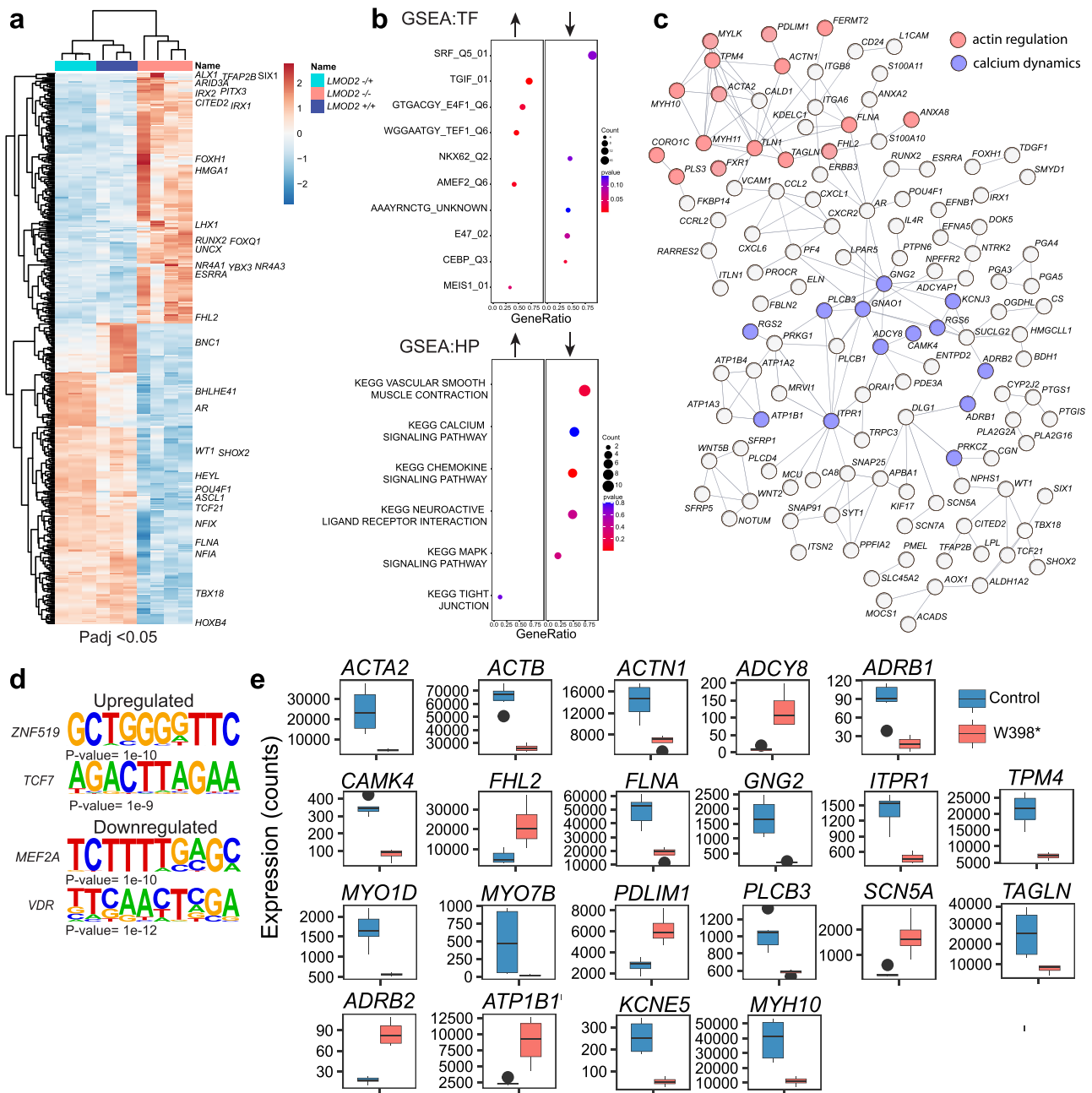
Fig. 7 | Bulk RNA sequencing of *LMOD2* W398* hiPSC-CMs demonstrates significant changes in transcriptomic signatures related to myofilament, transcription factor, and calcium-regulatory genes. **a** Heatmap analysis generated from bulk RNA-seq showing differentially expressed genes (DEGs) between control and *LMOD2* W398* hiPSC-CMs with transcription factor-related genes annotated. $N = 3$ *LMOD2*$^{+/+}$, $N = 3$ *LMOD2*$^{-/+}$, $N = 4$ *LMOD2*$^{-/-}$ W398* hiPSC-CMs. **b** Gene set enrichment analysis (GSEA) demonstrating significant upregulated and downregulated transcription factor (TF) and human phenotype (HP)-related genes identified between control and *LMOD2* W398* hiPSC-CMs, $N = 4$–6 independent cardiac differentiations. **c** STRING network analysis of DEGs showing protein-protein interactors, with proteins involved in actin regulation displayed in red and calcium dynamics in blue. **d** Motif Enrichment Analysis (MEA) for upregulated and downregulated genes derived from DEGs between control and *LMOD2* W398* hiPSC-CMs. **e** Gene expression profiles of significant actin regulatory genes identified between control and *LMOD2* W398* hiPSC-CMS, $N = 4$–6 independent cardiac differentiations, padj < 0.05. Box and whisker plots show median (horizontal line), standard deviation (box) and maximum and minimum values (whiskers).

sarcomere: (1) Lmod2 could be altering the overlap of thin and thick filaments through its regulation of actin-thin filament lengths (as observed by a decrease in thin filament lengths in *LMOD2* W398* hiPSC-CMs and *Lmod2* W405* mice), (2) phosphorylation profiles of thin filament regulatory proteins or calcium channels could be altered when *LMOD2* is mutated or, (3) Lmod2 is known to have a tropomyosin binding site[46] and the ability to bind the side of actin filaments, therefore it could be that Lmod2 is affecting overall contraction through its interaction with

tropomyosin or through inhibition of myosin ATPase activity when bound to actin filaments[47]. These predictions remain to be examined, however, immunoblot analysis in this manuscript detected no significant change in the expression levels of channels regulating calcium influx (L-type calcium channel, ryanodine, and calsequestrin) or efflux (sodium-calcium exchanger, phospholamban, and SERCA2a) in W398* hiPSC-CMs or D70 W405* mouse heart tissue. Interestingly, expression of CASQ2 was significantly increased in D20 *Lmod2* W405* heart tissue, possibly suggesting there may
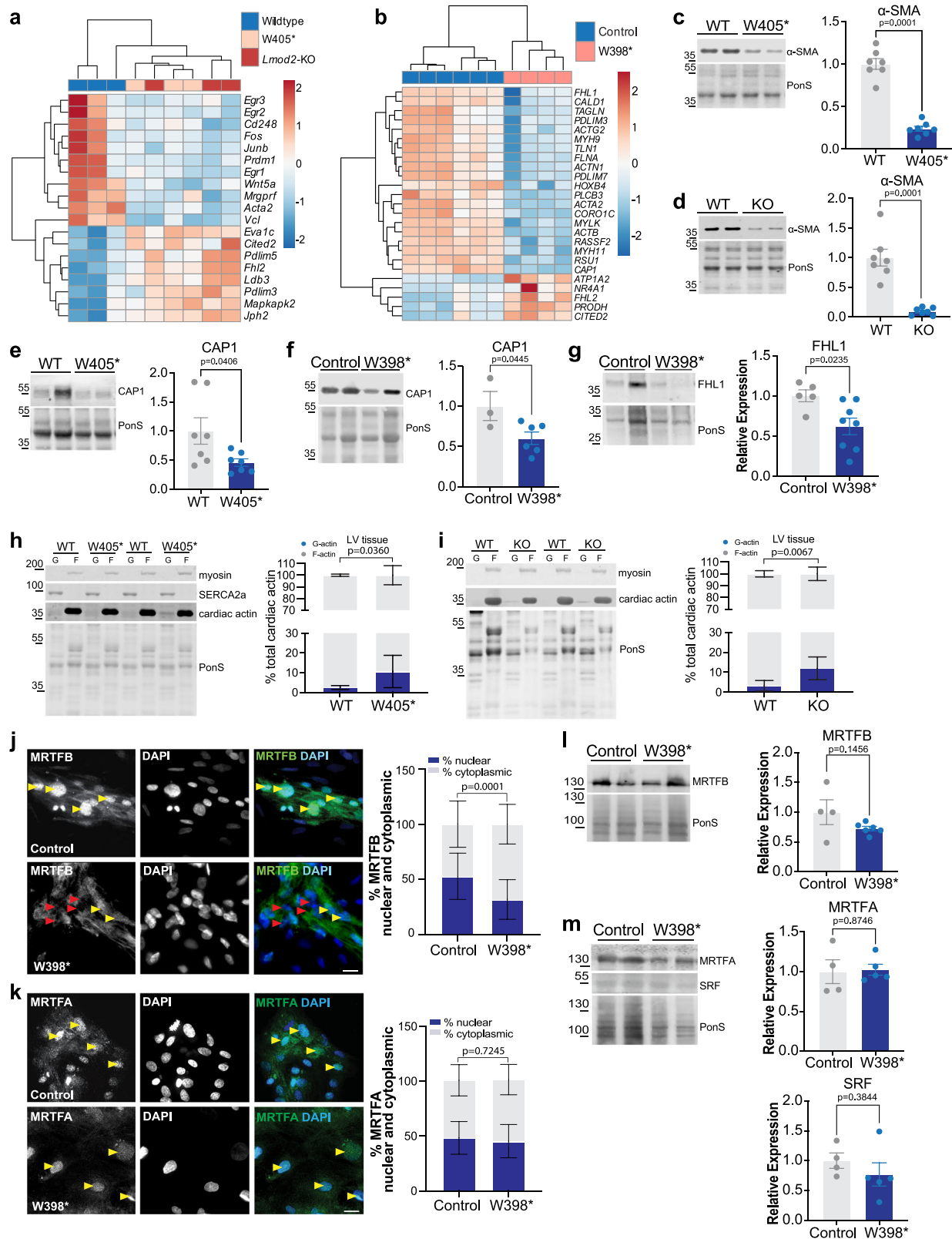
be an initial compensatory response for the reduced availability of systolic Ca²⁺. However, this trend did not hold true later in the disease process (at D70), implying there may be other upstream effectors (e.g., β-adrenergic signaling and PKA phosphorylation) modifying calcium channel function and contractility. To further explore the cause of calcium dysregulation, the expression of various phosphorylation sites on PLN, RyR2, and PKA were

examined, however, no statistical difference was detected in *Lmod2* W405* heart tissue. This indicates that the calcium-contraction pathway may be altered by other calcium regulatory elements (e.g., phosphorylation of CAMKII or cTnI S22/23, PKC activation, β-adrenergic activity, etc). This is supported by RNA-seq data from mutant hiPSC-CMs demonstrating a significant reduction in upstream calcium regulatory genes (e.g., *ADRB1*,

Fig. 8 | Mutant mouse LV tissue and hiPSC-CMs have downregulated SRF targets, a significant increase in G-actin levels, and/or decreased MRTFB but not MRTFA nuclear localization. Heat map demonstrating fold change in overlapping SRF downstream target genes in *Lmod2*-KO and *Lmod2* W405* mouse LV tissue (**a**) and mutant hiPSC-CMs (**b**). Immunoblot analysis of MRTF-SRF downstream targets: α-SMA in *Lmod2* W405* (**c**) and *Lmod2*-KO day 20 LV tissue (**d**), CAP1 in *Lmod2* W405* day 20 mouse LV tissue (**e**) and mutant hiPSC-CMs (**f**), and FHL1 in mutant hiPSC-CMS (**g**). Immunoblot analysis for globular (G-actin, G) and filamentous (F-actin, F) cardiac actin and corresponding quantification of immunoblots demonstrating the percentage of cardiac F-actin and G-actin in day 70 *Lmod2* W405* LV tissue (**h**) and day 14 *Lmod2*-KO LV tissue (**i**). Values are means ± s.d.,

N = 3 independent cardiac differentiations, *n* = 6 *Lmod2* W405* LV tissue, *n* = 6 *Lmod2*-KO LV tissue, Student's *t*-test, two-tailed. Representative immunofluorescence images of MRTFB (**j**), MRTFA (**k**), SRF, and nuclei (DAPI) with corresponding quantification of % nuclear and % cytoplasmic localization in hiPSC-CMs. Yellow arrows indicate MRTFA/B nuclear localization and red arrows indicate undetected nuclear localization of MRTFB. Values are means ± s.d., Student's t-test, two-tailed, *N* = 3 cardiac differentiations, scale bar = 1.0 µm. Immunoblots and corresponding quantifications of MRTFB (**l**), MRTFA, and SRF (**m**) in *LMOD2* W398* and control hiPSC-CM whole cell lysate. Relative expression levels were determined following normalization to Ponceau S (PonS). Values are means ± s.e.m., *N* = 3–6 independent cardiac differentiations, Student's *t*-test, two-tailed.

ATP1B1, and *CAMK4*) but not calcium channels (e.g., *RYR, PLN*, and *ATP2A2*). Further exploration is necessary into the detailed mechanism of calcium-contraction handling.

The pathogenesis of DCM is complex and the precise molecular mechanism underlying disease pathology is not well understood, especially regarding dysregulation of thin filament proteins. Previous studies have attempted to assess the contractile, electrical, and calcium properties of thin filament-associated DCM-causing mutations[48]. However, differing effects have been observed owing to differences in strain/model system, type of mutation, affected thin filament protein, and severity of mutation[48]. Interestingly, RNA-seq performed in mutant hiPSC-CMs and both *Lmod2* W405* and *Lmod2*-KO mouse models collectively identified the downregulation of the serum response factor (SRF) pathway. SRF is a critical transcription factor that regulates cardiomyocyte maturation by directly activating genes involved in sarcomere assembly, calcium homeostasis, and muscle energetics (for reviews[21,31]). SRF can be coactivated by MRTFs, which respond to changes in actin dynamics[39]. MRTFA is expressed ubiquitously while MRTFB is predominantly expressed in cardiac muscle and blood vessels[49]. In this manuscript, we demonstrated that MRTFB, but not MRTFA, has decreased nuclear localization in hiPSC-CMs and perinuclear localization in *Lmod2* W405* mice. Although the significance of perinuclear localization is unclear, we speculate it is a result of altered MRTFB translocation. Due to the presence of three tandem RPEL repeats located on the N-terminus of MRTFs, they are responsive to changes in G- and F-actin levels, such that binding of monomeric G-actin to these motifs, results in the inhibition of MRTF translocation into the nucleus[39]. Alterations in MRTF nuclear translocation due to changes in G-/F-actin ratios have been previously described in several cardiac disease types. Increased G-/F-actin ratios due to actin disassembly were reported with multiple DCM-causing mutations in lamin A/C *(LMNA)*[50,51], α-actinin-2 *(Actn2)*[52], and cyclase-associated protein 2 *(Cap2)*[24] as well as in a volume overload heart failure model[53]. Alternatively, increased F-/G-actin ratios have been described in several cardiac disease states including hypertrophic cardiomyocytes[54–56], diabetic cardiomyopathy[57], and in a hyperfibrotic model with cardiac fibroblasts[58]. Our studies demonstrated that *Lmod2* W405* mice and *Lmod2*-KO mice had significant increases in cardiac G-actin. These findings potentially explain the decreased MRTFB nuclear localization observed in hiPSC-CMs and the increased perinuclear localization in *Lmod2* W405* mice. Furthermore, the percentage of MRTFB protein associated with G-actin was significantly increased in LV tissue from *Lmod2* W405* and *Lmod2*-KO mice, further supporting the accumulation of MRTFB in the cytoplasm. If this is the case, less MRTFB would be available to activate SRF in the nucleus and the expression of downstream target genes would be reduced.

Our mutant hiPSC-CMs demonstrated dysregulation of several MRTF-SRF-regulated genes (for a comprehensive list of MRTF-SRF genes see ref.[31]) involved in microfilament building (*ACTA2, ACTB,* and *ACTG2*), actomyosin structure and regulation (*MYH11, MYH9, and MYLK*), muscle cell contraction (*TAGLN* and *CALD1*), transcriptional regulation (*FHL1*), and integrin signaling (*TLN1* and *FLNA*). Similarly, *Lmod2* W405* and *Lmod2*-KO mice demonstrated downregulation of several downstream MRTF-SRF targets (e.g., *Cap1, Acta2,* and *Vcl*). Of these, *Acta2* expression

was significantly downregulated in both mutant mouse models and in hiPSC-CMs, which is expected with SRF downregulation. Interestingly, the expression of *Fhl2* was significantly upregulated in all models. We predict this is a consequence of FHL2's diverse functions; FHL2 has an antagonistic effect on MRTF-mediated SRF signaling, FHL2 competes with MRTFA for SRF binding, and has an autoinhibitory effect on SRF activity[59,60]. Therefore, it may be that dysregulation of *ACTA2* and/or *FHL2* could be involved in the pathogenesis of the *W398* mutation. Future studies examining the transcriptional regulation of these two genes and their downstream effects should be considered.

Transcriptomic and protein analysis further revealed an upregulation of several sarcomeric proteins, particularly Z-disc and intercalated disc proteins (e.g.,*Tcap, Nrap*, and *Flnc*), in *Lmod2* W405* and *Lmod2*-KO mice. We speculate the increase in Z-disc proteins may be a result of myofibrillogenesis due to eccentric hypertrophy, characteristic of DCM pathogenesis, as NRAP and filamin C are early myofibril precursors in the assembly of myofibrils (for review[61]). Additionally, NRAP upregulation has been reported in several DCM mouse models (CSRP3/MLP knockout mice and tropomodulin overexpressing transgenic mice), likely as a result of impaired myofibrillar function and physiological stress.[62] Likewise, the stress generated at the actin-myosin complex can trigger intrinsic mechanosensing proteins at the Z-disc as an adaptive and compensatory response to an insult on the myocardium[63].

The indispensable role of SRF in regulating actin cytoskeletal dynamics, cardiac development, and cell growth, as well as its implications in cardiovascular disease, have been well documented[64–66]. When heart-specific deletion of SRF in mouse embryos was studied, it resulted in multiple cardiac pathologies including thin myocardium, dilated cardiac chambers, poor trabeculation, and disorganized interventricular septums, ultimately resulting in embryonic lethality[65]. Therefore, SRF is at the intersection of many integral pathways responsible for cardiogenesis and cardiac homeostasis. Based on the known functions of the SRF pathway, in addition to our data supporting alterations in MRTFB nuclear localization and increased levels of G-actin in mutant cells/tissue, we propose a new model of how the *LMOD2* W398* mutation may be involved in SRF regulation and disease pathology (Fig. 10). Under normal conditions, Lmod2 functions as an elongation factor, working with Tmod1 to precisely fine-tune thin filament lengths (for review[67]). However, when mutated, Lmod2 function is perturbed leading to decreased actin polymerization and increased levels of monomeric G-actin. This results in binding of G-actin to MRTF and inhibition of its nuclear localization signal, thus preventing MRTF from translocating into the nucleus and activating SRF-targeted genes. Therefore, Lmod2 could be regulating MRTF translocation in an actin-dependent manner. If so, downstream dysregulation of the MRTF-SRF pathway would contribute to alterations of targeted muscle-specific gene expression, inducing fetal reprogramming of cells and alterations in contractile, calcium, and cytoskeletal properties of cardiomyocytes. If Lmod2 affects SRF activation, a therapeutic potential targeting SRF or its cofactors via small molecules or pharmacological agents could potentially offer future treatment options. This is critical as the number of lethal DCM-causing *LMOD2* mutations discovered in neonates and infants is growing[16–19].
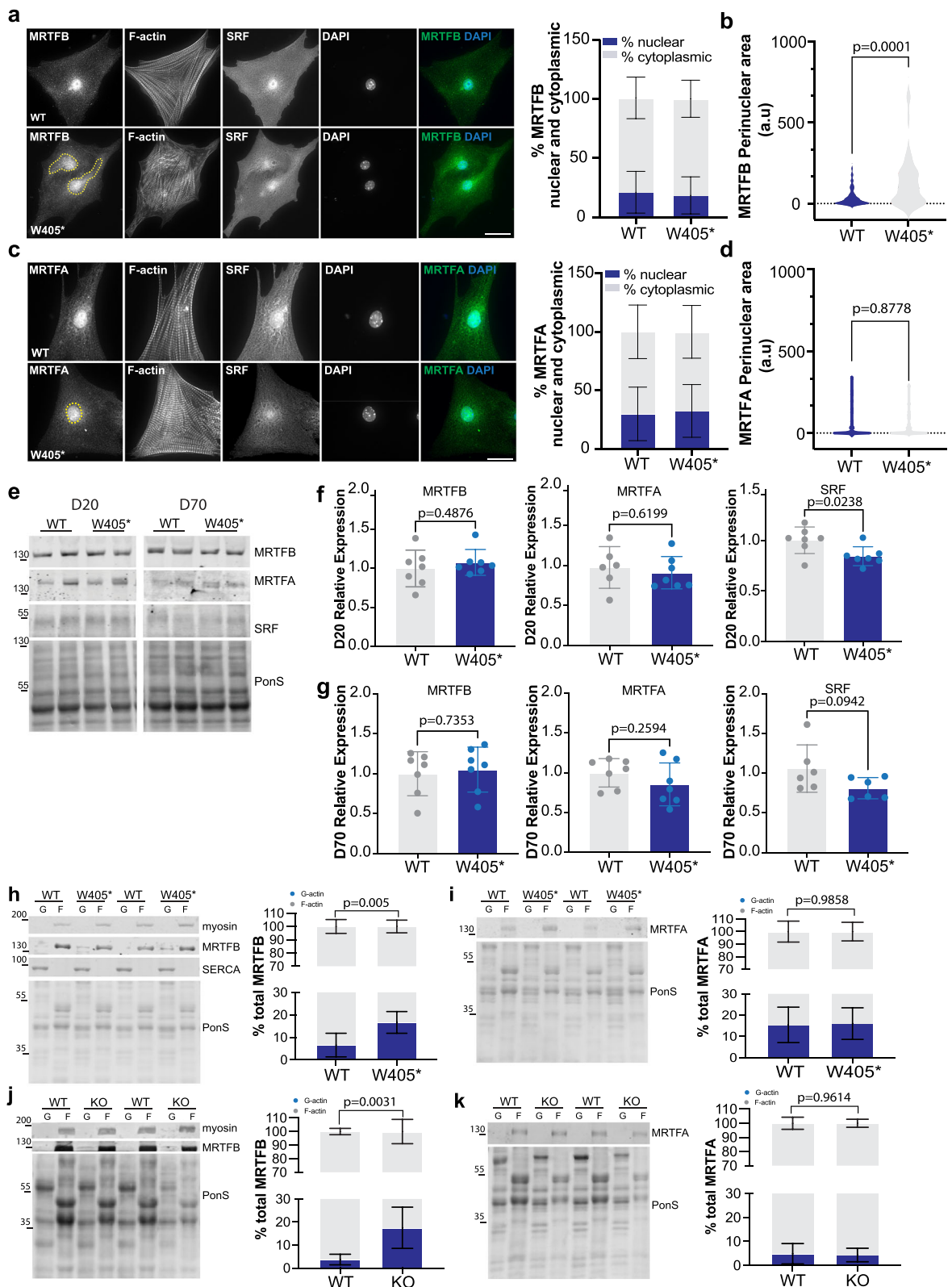
Methods

Generation of hiPSC-CMs and CRISPR/Cas9 isogenic controls

Blood collected from the patient, with written informed consent under IRB# 16-13231 at the Children's Hospital of Philadelphia (in compliance with all relevant ethical regulations including the Declaration of Helsinki) was used to generate peripheral blood mononuclear cells (PBMCs), which were then reprogrammed into iPSC lines using a Sendai virus vector carrying Oct3/4, Sox2, Klf4 and c-Myc transcription factors[68]. In brief, iPSC lines were differentiated into cardiomyocytes using a monolayer, small molecule biphasic Wnt-based approach, as previously described[22].

To generate isogenic corrected LMOD2 iPSC lines, CRISPR/Cas9 was performed using a modified protocol within the University of Arizona iPSC

Fig. 9 | MRTFB has increased fractionation with cardiac G-actin in *Lmod2* mutant mouse heart tissue. a Representative immunofluorescence images of MRTFB, SRF, and nuclei (DAPI) with corresponding analysis of % nuclear and % cytoplasmic localization in isolated neonatal cardiomyocytes from wild-type and *Lmod2* W405* mice. **b** Violin plot of MRTFB perinuclear distribution in wild-type and *Lmod2* W405* isolated neonatal cardiomyocytes. **c** Representative immuno-fluorescence images of MRTFA and corresponding analysis of % nuclear and % cytoplasmic localization. a.u arbitrary units. **d** Violin plot of MRTFA perinuclear distribution in wild-type and *Lmod2* W405* isolated neonatal cardiomyocytes. Values are means ± s.d., $N = 3$ independent cultures, Student's *t*-test, two-tailed. Yellow dashed lines indicate nuclear and perinuclear localization of MRTFA and MRTFB, respectively. Scale bar = 1.5 μm. **e** Immunoblots demonstrating MRTFA,

MRTFB and SRF expression in heart tissue (LV) lysate from wild-type and *Lmod2* W405* mice at day 20 (D20) and 70 (D70) with corresponding quantification of D20 (**f**) and D70 (**g**). Relative expression levels were determined following normalization to Ponceau S. Values are means ± s.d., $n = 7$ control and *Lmod2* W405* LV tissue samples, Student's *T*-test, two-tailed. Immunoblot analysis for globular (G-actin, G) and filamentous (F-actin, F) cardiac actin with corresponding quantification demonstrating the percentage of MRTFB (**h**) or MRTFA (**i**) in F-actin and G-actin fractions in *Lmod2* W405* LV mouse tissue. Immunoblot analysis for G-actin and F-actin with corresponding quantification demonstrating the percentage of MRTFB (**j**) and MRTFA (**k**) in wild-type and *Lmod2*-KO LV tissue samples. Values are means ± s.d., $n = 6$ LV tissue samples. Student's *t*-test, two-tailed.
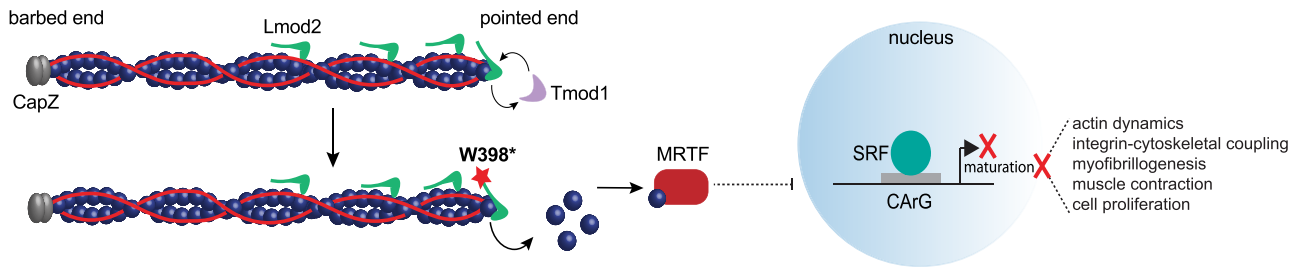

Fig. 10 | Proposed mechanism of SRF regulation by Lmod2 in cardiomyocytes. Schematic demonstrating under wild-type conditions Lmod2 and Tmod1 fine-tune tropomyosin-decorated thin filaments by acting as an elongation factor and capping protein, respectively. When Lmod2 is mutated, actin polymerization is perturbed and results in increased monomeric G (globular)-actin which binds to the actin-binding site on myocardin-related transcription factor (MRTF) and subsequently prevents MRTF translocation into the nucleus and thus activation of SRF-dependent target genes involved in cardiomyocyte function and maturation.

Core. In brief, 250 000 cells were transfected with 1.65 μL of 63 μM Cas9, 4 μL RNAiMax, 1.65 μL of 100 μM guideRNA (GGGGA-GUUUUGGGGAUGACU) and 1.65 μL of 100 μM donor ssODN (acgatggaggacccaatcttaggaccaaagtctggcaaagaggaacacctagctcttcaccttatgtatctc ccaggcactcaccctggtcatccccaaaactccccaaaaaagtccagactgtgag). Four days after transfection, cells were seeded at a cell density of 2000 cells per 6-well dish. After culturing for twelve days, colonies were picked, expanded, and sequence-verified using Sanger sequencing.

Immunofluorescence microscopy and thin filament length analysis

A section of LV free wall from *Lmod2* W405* mice was fixed overnight in 4% (wt/vol) paraformaldehyde/PBS, washed in PBS, embedded in Tissue-Tek O.C.T (Sakura Finetek) and subsequently frozen in 2-methylbutane cooled in liquid N_2. Cryosections of LV tissue were mounted onto number 1.5 coverslips and processed as described below. Additionally, day 30 hiPSC-CMs cultured on Matrigel-coated ibidi plates (Ibidi, #81156) and day 4 wild-type/W405* mouse isolated neonatal cardiomyocytes (see cell isolation and mouse cultures below) were washed twice with 1xPBS and incubated in relaxing buffer (150 mM KCl, 1 mM, 5 mM MgCl₂, 1 mM EGTA, 10 mM M OPS, PH 7.4, and 4 mM ATP) for 15 mins at room temperature. Cells were then fixed with 2% (wt/vol) paraformaldehyde in relaxing buffer for an additional 15 mins at room temperature and subsequently stored in PBS at 4°C and processed as described below.

On the day of staining, cells or cryosections of LV tissue were permeabilized in 0.2% Triton X-100 in 1XPBS for 20 mins at room temperature and then blocked with 2% BSA, 1% normal donkey serum in 1XPBS for 1 h at room temperature. Primary antibodies (see Table 1) were incubated overnight at 4 C. The next day, cells or cryosections were washed with 1XTBST 4 x 5min and incubated with secondary antibodies, which included Alexa Fluor 405-conjugated goat anti-mouse IgG (1:200), Alexa Fluor 488-conjugated goat anti-rabbit IgG (1:300), Alexa Fluor 488-conjugated don-key anti-mouse IgG (1:300), Alexa Fluor 594-conjugated goat anti-rabbit IgG (1:300), Alexa Fluor 594-conjugated goat anti-mouse IgG (1:300), and Texas Red™-X Phalloidin (1:100) (Thermo Fisher Scientific) for 1.5 h at room temperature. Cells or cryosections were then washed with 1XTBST 4 x 5min and mounted with Aqua Poly/Mount (Polysciences). Images of cultured cells were taken using a Nikon Eclipse Ti microscope with a ×10 NA 0.3 or ×100 NA 1.5 objective, and a digital CMOS camera (ORCA-flash4.0, Hamamatsu Photonics, Shizuoka Prefecture, Japan) and 3D deconvolution was performed using NIS offline deconvolution software (Nikon Corporation, Tokyo, Japan). Images of LV tissue sections were captured using a Deltavision RT system (Applied Precision) with a ×100 NA 1.3 objective and a CCD camera (CoolSNAP HQ; Photometrics) and deconvolved using SoftWoRx software. Thin filament lengths were measured using the Ddecon plugin for ImageJ[69].

Coherency and line scan analysis in hiPSC-CMs and *Lmod2* W405* LV tissue

Immunofluorescence images of hiPSC-CMs and *Lmod2* W405* LV tissue stained for anti-α-actinin were imported into Fiji and transformed to ver-tically orient the image. The plugin, OrientationJ[70], was used to measure coherency (a measure of myofibril alignment). The coherency index indi-cates the degree to which the myofibrils are oriented. The values are set from 0.1 to 1.0, where 1.0 is the maximal coherency. Multiple measurements were taken from each cell (at least 5 measurements in different areas of a cell) and the average coherency value per cell was calculated. Line scan analysis of F-actin and/or α-actinin staining was performed using ImageJ.

Protein extraction and immunoblot analysis

hiPSC-CMS or mouse cardiomyocytes were washed twice with 1xPBS and scraped off gelatin-coated plates in cold lysis buffer (25 mM HEPES, pH 7.4, 150 mM NaCl, 1.5 mM MgCl₂, 1 mM EGTA, 10 mM sodium pyropho-sphate, 10 mM sodium fluoride, 0.1 mM sodium deoxycholate, 1% Triton X-100, 1% SDS, 10% (vol/vol) glycerol, 1X Halt Protease Inhibitor Cocktail [ThermoFisher Scientific, 78439]). Cell lysate was then sonicated and spun down at 16,000 x *g* for 15 min at 4 °C. Total lysate protein concentration was normalized using the Pierce BCA protein assay kit (Thermo Fisher Scien-tific) and samples boiled in 1X Laemmli sample buffer at 100 °C for 10 min. Lysate was resolved on a 10% or 12% SDS gel and transferred to an Immobilon-FL PVDF membrane (0.45 μm, Thermo Fisher Scientific). Membranes were subsequently blocked in 5% (wt/vol) nonfat dried milk in 1xTBST for 1 h at room temperature and incubated at 4 °C overnight with primary antibodies diluted in 2% BSA in 1xTBST (see Table 1 for a

Table 1 | List of antibodies used in experiments

ANTIBODY	SPECIES	DILUTION	VENDOR	USE
anti-Lmod2	rabbit	1:1000/ 1:100	Santa Cruz Biotechnology, E13	IB/ ICC
anti-CAP2	rabbit	1:2000/ 1:100	Proteintech, 15865-1-AP	IB/ ICC
anti-Tmod1	rabbit	1:20 000/ 1:2000	(0.2 µg/mL)[76]	IB/ ICC
anti-α-Actinin	goat/ mouse	1:400/ 1:200	R&D Systems, AF8279/Sigma-Aldrich, EA-53	IB/ ICC
anti-Myosin binding protein-c	rabbit	1:500	Myomedix, MYBPC3-1C	IB
anti-Cardiac actin	mouse	1:1000	American Research Products, Inc, 03-61075	IB
anti-Tropomyosin-1	mouse	1:1000	Novus Biologicals, TM311	IB
anti-Lmod3	rabbit	1:1000	Proteintech, 14948-I-AP	IB
anti-Myc	mouse	1:1000/ 1:200	Cell Signalling, 9811	IB/ ICC
anti-β-Actin	mouse	1:1000	Sigma-Aldrich, A1978	IB
anti-Troponin T	mouse	1:200	Sigma-Aldrich, JLT-12	IB
anti-SERCA2a	rabbit	1:1000	Badrilla, A010	IB
anti-Calsequestrin-2	rabbit	1:1000	Proteintech, 18422-1-AP	IB
anti-MF20/59	mouse	1:50	Hybridoma Bank	IB
anti-Slow skeletal troponin I	rabbit	1:500	Santa Cruz, sc30490	IB
anti-Cardiac troponin I	mouse	1:500	Covance, Mab20	IB
anti-MRTFA	rabbit	1:1000	Cell Signalling, 14760	IB
anti-MRTFA	rabbit	1:200	Generous gift from Dr. Eric Small	ICC
anti-MRTFB	rabbit	1:1000/ 1:100	Cell Signalling, 14613	IB/ ICC
anti-SRF	mouse	1:500/ 1:200	Santa Cruz, sc-25290	IB/ ICC
anti-Phospholamban	rabbit	1:500	Badrilla, A010-13	IB
anti-Sodium/calcium exchanger	mouse	1:500	Thermos Fisher Scientific, MA3-926	IB
anti-Ryanodine-2	mouse	1:1000	Sigma-Aldrich, R129	IB
anti-Ryanodine-2-pSer^{2814}	rabbit	1:1000	Badrilla, A010-31	IB
anti-Ryanodine-2-pSer^{2808}	rabbit	1:2500	Badrilla, A010-30	IB
anti-PKA [RIIα]	mouse	1:1000	BD Biosciences, 612242	IB
anti-PKA [RIIβ]	mouse	1:1000	BD Biosciences, 610165	IB
anti-Phospholamban-pThr^{17}	rabbit	1:1500	Badrilla, A010-13	IB
anti-Phospholamban-pSer^{16}	rabbit	1:3000	Badrilla, A010-12	IB
anti-α-Smooth-Muscle-actin	mouse	1:1000	Sigma-Aldrich, A2547	IB
anti-FHL1	mouse	1:1000	Abcam, 76912	IB
anti-CAP1	mouse	1:500	Santa Cruz, sc-376286	IB
anti-α-Skeletal-Muscle-actin	mouse	1:1000	Exalpha Biologicals Inc, MUB0108P	IB
anti-NRAP	rabbit	1:1000	Invitrogen, PAS-58183	IB
anti-FLNC	rabbit	1:1000	Myomedix	IB
anti-FHL2	mouse	1:1000	MBL International, K0055-3	IB

IB immunoblot, *ICC* immunocytochemistry.

comprehensive list of antibodies used). Following 5 x 10 min washes in 1xTBST, membranes were incubated for 1.5 h at room temperature with fluorescently labeled secondary antibodies including Alexa Fluor 680 or Alexa Fluor 790 AffiniPure donkey anti-rabbit or mouse immunoglobulin G (IgG) (1:40,000; Jackson ImmunoResearch). Blots were imaged and analyzed using the Odyssey CLx imaging system (LI-COR Biosciences). Relative expression levels were determined following normalization to Ponceau S (PonS). The decision to use PonS, as opposed to other housekeeping proteins for normalization (e.g., α-actin, GAPDH), was made to avoid the use of a housekeeper that may be compromised by the cytoskeletal mutation under study.

Calcium ion transient and cell contraction analysis
For intracellular Ca^{2+} transient recordings, day 30 hiPSC-CMs or isolated mouse neonatal cardiomyocytes cultured on 35 mm Matrigel-coated Mat

Tek culture dishes (Thermo Fisher Scientific) were incubated with 5 µM Fura-2-AM (Life Technologies) for 30 min at 37 °C. Following incubation, cells were washed once and then incubated in cardiac media for an additional 15 min at 37 °C. This allowed for complete de-esterification of intracellular Fura-2 and re-balancing of calcium handling properties prior to Ca^{2+} imaging. Recordings of Ca^{2+} transients from hiPSC-CMs or mouse cardiomyocytes were taken at 37 °C while pacing at 1 Hz (Myopacer field stimulation element, IonOptix LLC, United States) using the CytoCypher Microscope Module with 35 mm dish insert and the CytoCypher System Control Module (Cytocypher, BV, Netherlands). Cells were excited at 340 nm and 380 nm and fluorescence emission was collected at 510 nm. The ratio of 340/380 nm was used to generate Ca^{2+} peaks over time (s). Data was collected using the IonOptix IonWizard 7.3 program (IonOptix LLC, United States) and then exported and analyzed in IonOptix's Transient Analysis Software Tool 1.2.97.0. Concurrently while recording Ca^{2+}

transients, video optical recordings (4 s) of hiPSC-CMs or mouse cardiomyocytes were taken along the long axis of cells. Videos were then exported in .avi format to an open-source software tool, MUSCLEMOTION[25], for contraction analysis. Standard settings were used in the MUSCLEMOTION software per manufacturer's recommendations, with adjustments of the frame rate and speed window to match the rate at which the recordings were taken. Analysis of output parameters- contraction amplitude, contraction duration and peak-to-peak time were performed by averaging values from a single cell recorded for 4 s at 1 Hz.

Generation of hiPSC-CM Engineered Heart Tissues (EHTs)

hiPSC-CM engineered heart tissues were generated with newly differentiated iPSC-derived cardiomyocytes dissociated from a 6-well plate and counted (1×10^6 hiPSC-CMs were used per EHT construct). In the meantime, an agarose mold was prepared by pipetting 1.5 mL of 2% (wt/vol) agarose in 1xPBS into a Nunc 24-well plate (Thermo Fisher Scientific, #144530) and placing Teflon spacers (EHT Technologies) into the agarose. After 15 min, Teflon spacers were removed from the agarose, leaving behind a mold. A master mix consisting of 1X DMEM (Thermo Scientific Fisher), Matrigel and fibrinogen (Sigma, #F8630) was prepared and separate thrombin (Sigma, #T7513) aliquots were made for the generation of each individual EHT. hiPSC-CMs were suspended in cardiac media and added to the master mix above. Subsequently, 97 μL of master mix was pipetted into the thrombin aliquot (3 μL) and promptly dispensed into the agarose mold containing a PDMS post (EHT Technologies). This process was repeated for the generation of each individual EHT, ensuring to proceed quickly prior to fibrin polymerization. EHT plates were placed into the incubator (37 °C, 5% CO_2) for 2 h. Following incubation, 500 μL of cardiac media was pipetted into each EHT and placed back into the incubator for an additional 15 min, to ease removal of EHTs from the agarose mold. EHTs were fed daily with cardiac media supplemented with aprotinin (GoldBio, #A-655-100). Contraction of EHTs was noted after 3–5 days and precisely one week after EHT generation, EHTs were started on an electrical pacing protocol at 0.5 Hz. Pacing was increased by 0.1 Hz daily until 1 Hz was reached, afterwards pacing was increased by 0.2 Hz daily. Video optical recordings of EHTs were taken for 15 s at 50fps to monitor contraction over time and .avi files were exported into the open-source contraction software, MUSCLEMOTION, as described above.

RNA isolation from hiPSC-CMs and mouse tissue for bulk RNA-sequencing

For bulk RNA-seq, hiPSC-CMs and mouse heart (LV) tissue were lysed using TRIzol reagent (Zymo Research) and total RNA was extracted using the Direct-zol RNA Miniprep Plus kit (Zymo Research). During RNA isolation, on-column DNAse digestion was performed for 15 min at room temperature. RNA-seq library prep using the Illumina TruSeq stranded mRNA kit and sequencing using a NovaSeq (PE150) system was performed at MedGenome Inc., CA. Fastq files were aligned using STAR to Ensembl GRCh38 annotation for human samples and Ensembl GRCm38 annotation for mus musculus samples. Differentially expressed genes were calculated using DESeq2, and heatmaps were generated using heatmap.2 plugin in RStudio packages. Gene set enrichment analysis (GSEA) was used to determine gene ontology and transcription factor enrichment terms for hiPSC-CMs and mouse heart tissue. The search tool for retrieval of interacting genes STRING database was used for protein-protein association network analysis[71] and HOMER (Hypergeometric Optimization of Motif EnRichment) was used to perform motif enrichment analysis[72].

MRTFA/B nuclear versus cytoplasmic quantification and perinuclear analysis

Day 30 hiPSC-CMs or day 4 WT/W405* mouse isolated cardiomyocytes were washed with 1XPBS and fixed with 2% paraformaldehyde in 1XPBS for 20 min at room temperature. Immunostaining procedures were then followed as described above. To calculate the percentage of MRTFA/MRTFB in the nucleus versus the cytoplasm, immunofluorescence images with staining against MRTFA or MRTFB and Hoescht were imported into the Intensity Ratio Nuclei Cytoplasm Tool in ImageJ (RRID: SCR_018573). For perinuclear analysis of MRTFA or MRTFB immunofluorescence image files were imported into ImageJ. The hoescht channel was used to apply a mask (Otsu method) to select for nuclei. An ROI was generated in the MRTF channel and the area of MRTF was calculated. Subsequently, the area of MRTFA or MRTFB was calculated by subtracting the area of the nucleus to obtain a final measurement of perinuclear area per cell.

Generation of the CRISPR/Cas9 knock-in W405* Lmod2 mouse model

The W405* Lmod2 mouse model was generated by the University of Arizona GEMM (Genetically Engineered Mouse Models) Core as follows: CRISPR guide RNAs, used for mouse Lmod2 gene W405X knock-in were designed using CRISPR.mit.edu. Four guides were selected and produced by PCR using as a template an Addgene pX330 plasmid, carrying the scaffold portion of the guide. The forward primer consisted of a T7 promoter sequence and the target sequence. sgRNAs (single guide RNAs) were designed to target the following sequences in the Lmod2 gene: GGAGACTTTGGGAGATGACCAGG (gRNA1), GAGACTTTGGGAGATGACCAGGG (gRNA2), GATGACCAGGGAGACTGTCTCGG (gRNA3) and GTGGACTTTCTTGGAGACTTTGG (gRNA5). sgRNAs were made by in vitro transcription using Ambion's MEGAshortscript kit and afterwards purified with MEGAclear kit. Cas9 protein was ordered from PNA Bio (CP01-50, USA) and used to check cutting efficiency of the guides in vitro, and for the purposes of the electroporation method. ssODNs with 60–70 bp homology to sequences on each side of each gRNA-mediated double-stranded break were designed and ordered from IDT. Fertilized eggs were collected from the oviducts of super ovulated C57BL/6NJ females. The final concentrations for the electroporation mixture Cas9 protein/gRNA/ssODN were 250/300/1000 ng/μl respectively. The mixture was then centrifuged at 16,000 g for 15 min at 4 °C and 10 μl supernatant was transferred to a new nuclease free tube. For the preparation of Cas9 RNP (recombinant Cas9 protein binding with sgRNA), the solution was incubated at 37 °C for 15 min. The samples were put on ice and used for electroporation immediately. Embryos were washed in Opti-MEM media. 75–100 embryos were placed in 10 μl drop of Opti-MEM to which the electroporation reagent was added, and then transferred to a 1 mm cuvette. Electroporation was carried out using 7 pulses at 30 V (3 msec ON + 97 msec OFF). After that, embryos were returned to Opti-MEM medium and transferred to the oviduct of pseudo pregnant females. Tail-tipping of the newborn mice was utilized to purify DNA for genotyping by PCR, employing two screening primers: forward, 5'- AACAAGGAATATGGATAAACAGAGG and reverse, 5'-TTTCCTGTTGTTTAATGACTTCTGC, producing 347 bp band for the wild-type and two additional bands of 197 bp and 150 bp in the positive mice when restricted with MboI. sgRNA1 and the corresponding oligo were the successful ones in introducing the desired mutation.

Cell isolation and mouse cultures

Mouse cardiomyocytes were cultured as previously described[9,73]. In brief, cardiomyocytes from P3 or younger mice were isolated from hearts obtained from 3–6 mice. Two parallel cultures were completed to account for each genotype (either WT or W405*). Isolated cells were plated onto 35-mm tissue culture dishes with 12 mm round glass coverslips coated with 1:100 Matrigel (BD Biosciences) at 2.0×10^5 cells per culture dish. Cells were maintained in DMEM with 1 g/L glucose (Gibco), 10% (vol/vol) FBS (HyClone) and 1% penicillin/streptomycin (Cellgro) and fed every other day.

Echocardiography

Echocardiography (echo) was performed on conscious mice at postnatal day 21 (P21) and under isoflurane-induced anesthesia (with a target heart rate of 550 ± 50 bpm) at later time points. Transthoracic echo images were obtained with a Vevo 2100 High-Resolution Imaging System (VisualSonics) using a model MS-550D transducer array. Images were collected

and stored as a digital cine loop for off-line calculations. Standard imaging planes and functional calculations were obtained according to American Society of Echocardiography guidelines. M-mode images at the level of the papillary muscles were used to determine LV wall thicknesses, chamber dimensions and ejection fraction.

AAV injected *Lmod2* knockout and control mice were echoed consciously at P16-P18 and under isoflurane-induced anesthesia at P90-P120 (the latter within a target heart range of 550 ± 50 bpm). Transthoracic images were obtained using the Vevo 770 High-Resolution In Vivo Micro-Imaging System from Visual Sonics with a 707B transducer array and images were saved as digital loops for offline calculations. Standard imaging planes and functional calculations were obtained according to the American Society of Echocardiography guidelines. M-mode images at the level of the papillary muscles were used to determine LV wall thicknesses, chamber dimensions, and ejection fraction.

Adenovirus (Adv) and Adeno-associated virus (AAV) experiments

Adenovirus (Adv) expressing myc-tagged mouse Lmod2 and adeno-associated virus (AAV-2/9) expressing GFP or GFP-mouse Lmod2 were generated by the Viral Production Core Facility at the University of Arizona as previously described[9]. At postnatal day 4 (P4), following the administration of cryoanesthesia, 1.25×10^{12} genomic copies of virus diluted in 50 μL of sterile 1X PBS with 2.5 mM KCl, 1 mM MgCl2, 0.0001% Tween20, and 0.0001% Pluronic F-127 was injected into the pericardial cavity. Pericardial injections were favored since this route of administration concentrates the virus and, in our hands, yields more efficient cardiac expression. After recovery from cryoanesthesia, the mice were returned to their cages and monitored closely until collection at ~P28.

hiPSC-CMs cultured for a minimum of 30 days were transduced 2-3 days prior to experiments with adenovirus expressing myc-tagged full-length Lmod2 at a multiplicity of infection (MOI) of 5. A myc-tagged viral construct was used as opposed to a GFP-tagged construct to avoid interference with Fura2 signaling and calcium data collection, as described in ref. 74.

G-actin and F-actin fractionations

Heart tissue (left ventricle) obtained from day 70 wild-type and *Lmod2*-W405* mice or day 14 wild-type and *Lmod2*-KO mice was homogenized using a dounce and passed through a 25 G syringe to further disrupt the tissue. Tissue was then fractionated into globular and filamentous actin using the G-actin/F-actin In Vivo Assay Biochem Kit (Cytoskeleton, Inc.) per manufacturer recommendations. Briefly, solubilized lysate/tissue was placed into Lysis and F-actin Stabilization Buffer supplemented with ATP (1 mM) and 1X protease inhibitor, prewarmed to 37 °C, incubated at 37 °C for 10 min, and centrifuged at 350 x *g* for 5 min at room temperature, to remove cell debris. Supernatant was transferred into ultracentrifuge tubes. F- and G-actin were fractionated by ultracentrifugation at 100,000 *g* for 1 h at 37 °C. Pellets (F-actin) were solubilized in F-actin depolymerization buffer and incubated on ice for 1 h. SDS sample buffer was added to the solubilized pellet, boiled for 10 min at 100 °C and resolved on SDS-PAGE to quantify actin levels. Myosin and/or SERCA2a were used as internal controls to verify appropriate fractionation into G- and F-actin. Additionally, lysis conditions were initially tested per manufacturer recommendations, in cells with treatment of either 0.01% DMSO (control), 2 μM Lat A (Invitrogen), or 0.15 μM jasplakinolide (Santa Cruz Biotechnology) overnight, at 37 °C and harvesting cell lysates the following day as described above.

Force-calcium relationship experiments

Prior to sacrificing, mice were injected with 100 units of heparin and anesthetized with isoflurane. After 5 min mice were sacrificed by cervical dislocation. The heart was then excised, transferred to a dissection dish weighed and perfused retrograde with a modified Krebs-Henseleit solution, containing 118.5 mM NaCl, 5 mM KCl, 2 mM NaH 2 PO 4, 1.2 mM MgSO 4, 10 mM glucose, and 26.4 mM NaHCO3, as well as an additional 10 mM KCl to inhibit spontaneous contractions. This solution, when aerated at

room temperature with a 95% O 2 /5% CO2 mixture had a pH of 7.4. The intra-ventricular septum was removed and quickly frozen in liquid nitrogen for use later in single-cell experiments. The atria, RV outer wall and LV outer wall were also sectioned and frozen in liquid nitrogen for later protein analysis.

The compositions of all solutions used in force-calcium experiments have been previously reported[28]. Of note, activating solution and relaxing solution were mixed to obtain activating solutions containing between 1 and 46.8 μM [Ca 2] (pCa6.2–4.3).

Single-cell experiments were performed on an inverted microscope stage using an Aurora Scientific 803B permeabilized myocyte apparatus with some slight modifications. A 406 A force transducer was used to get a wider range of min and max forces. Permeabilized single cells were acquired by taking ~a third of the septum frozen during tissue collection and homogenizing the tissue in standard relaxing solution containing 1% Triton X-100. The cells were gently pelleted with centrifugation at 500 rpm for 3 min. The pellet was washed three times with standard relax solution to remove any remaining detergent and centrifugation was repeated. Once isolated, cells were glued between the motor arm and force transducer with silicone. After the glue dried, the diastolic SL was set to 2.25–2.30 microns and the Force/Calcium relationship was determined. Force/$[Ca^{2+}]$ relationships were fit individually to a modified Hill equation as previously described[75] to:

$$F_{rel} = [Ca^{2+}]^{n}/(EC_{50}{}^{n} + [Ca^{2+}]^{n}) \tag{1}$$

where F_{rel} = force as a fraction of maximum force at saturating $[Ca^{2+}]$ (F_{max}), $EC_{50} = [Ca^{2+}]$ where the F_{rel} is half of F_{max}, and n = Hill Coefficient.

Ethical use of animals

Work with animals was performed under the approval of The Institutional Animal Care and Use Committee at the University of Arizona, which confirmed all applicable federal and institutional policies, procedures, and regulations, including the PHS Policy on Humane Care and Use of Laboratory Animals, USDA regulations (9 CFR Parts 1, 2, 3), the Federal Animal Welfare Act (7 USC 2131 et. Seq.), the Guide for the Care and Use of Laboratory Animals, and all relevant institutional regulations and policies regarding animal care and use at the University of Arizona.

Inclusion and ethics

All listed authors fulfill authorship criteria and contributed to the manuscript as outlined in the "Contributions" section. This manuscript included local researchers throughout the research process to promote greater equity in research collaborations. Roles and responsibilities were agreed upon by collaborators ahead of the research project.

Statistics and reproducibility

Statistical analysis was performed in GraphPad Prism version 9.5.1 for macOS (GraphPad Software, Inc.) or RStudio. A two-tailed Student's *t*-test, one-way ANOVA or two-way ANOVA with Tukey's post-hoc test was used depending on the number of independent variables and groups used in each experiment. Normality was confirmed using the Shapiro-Wilk test for smaller data sets and the appropriate statistical test was used for parametric and non-parametric data as indicated in all figure legends. Statistical significance was considered when $p < 0.05$. Each experiment was completed with 3-6 independent iPSC differentiations from different clones or independent mouse cultures. All values are mean ± s.d, unless otherwise indicated. Data was compiled and statistical figures were generated in Prism 9.5.1. Final images were prepared using Adobe Illustrator. RStudio was used to generate dot plots and heat maps. GSEA (gene set enrichment analysis) was used to identify significant Gene Ontology terms (GO biological process, GO transcription factor, and GO human phenotype) with a padj<0.05.

Data availability

All data generated or analyzed during this study are included in this published article (and its supplementary information files). All relevant data are available from the corresponding author upon reasonable request. RNA-sequencing data has been deposited at GEO and is publicly available as of the date of publication under GEO accession number GSE271871.

Code availability

Public software and code were used to generate or process datasets in this manuscript. The software version and code used, along with the appropriate citation, were described in the "Methods" section.

References

1. Merlo, M. et al. Evolving concepts in dilated cardiomyopathy. *Eur. J. Heart Fail.* **20**, 228–239 (2018).
2. McNally, E. M. & Mestroni, L. Dilated Cardiomyopathy. *Circ. Res.* **121**, 731–748 (2017).
3. Khan, R. et al. Genetic Testing Outcomes in Pediatric Dilated Cardiomyopathy. *J. Hear. Lung Transplant.* **38**, S201 (2019).
4. Weintraub, R. G., Semsarian, C. & Macdonald, P. Dilated cardiomyopathy. *Lancet (Lond., Engl.)* **390**, 400–414 (2017).
5. Towbin, J. A. et al. Incidence, Causes, and Outcomes of Dilated Cardiomyopathy in Children. *JAMA* **296**, 1867 (2006).
6. Pugh, T. J. et al. The landscape of genetic variation in dilated cardiomyopathy as surveyed by clinical DNA sequencing. *Genet. Med.* **16**, 601–608 (2014).
7. Mi-Miid, L. et al. In vivo elongation of thin filaments results in heart failure. *PLoS One* https://doi.org/10.1371/journal.pone.0226138 (2020).
8. Skwarek-Maruszewska, A. et al. Different localizations and cellular behaviors of leiomodin and tropomodulin in mature cardiomyocyte sarcomeres. *Mol. Biol. Cell* **21**, 3352–3361 (2010).
9. Pappas, C. T. et al. Knockout of Lmod2 results in shorter thin filaments followed by dilated cardiomyopathy and juvenile lethality. *Proc. Natl Acad. Sci.* **112**, 13573–13578 (2015).
10. Chereau, D. et al. Leiomodin is an actin filament nucleator in muscle cells. *Science* **320**, 239–243 (2008).
11. Conley, C. A., Fritz-Six, K. L., Almenar-Queralt, A. & Fowler, V. M. Leiomodins: Larger Members of the Tropomodulin (Tmod) Gene Family. *Genomics* **73**, 127–139 (2001).
12. Nanda, V. & Miano, J. M. Leiomodin 1, a new serum response factor-dependent target gene expressed preferentially in differentiated smooth muscle cells. *J. Biol. Chem.* **287**, 2459–2467 (2012).
13. Halim, D. et al. Loss of LMOD1 impairs smooth muscle cytocontractility and causes megacystis microcolon intestinal hypoperistalsis syndrome in humans and mice. *Proc. Natl. Acad. Sci.* **114**, E2739–E2747 (2017).
14. Nworu, C. U., Kraft, R., Schnurr, D. C., Gregorio, C. C. & Krieg, P. A. Leiomodin 3 and tropomodulin 4 have overlapping functions during skeletal myofibrillogenesis. *J. Cell Sci.* **128**, 239–250 (2015).
15. Yuen, M. et al. Leiomodin-dysfunction results in thin filament disorganization and nemaline myopathy. *J. Clin. Invest.* **124**, 4693–4708 (2014).
16. Sono, R. et al. Whole-Exome Sequencing Identifies Homozygote Nonsense Variants in LMOD2 Gene Causing Infantile Dilated Cardiomyopathy. *Cells* **12**, 1455 (2023).
17. Lay, E. et al. LMOD2-related dilated cardiomyopathy presenting in late infancy. *Am J. Med Genet A* https://doi.org/10.1002/ajmg.a.62699 (2022).
18. Yuen, M. et al. Neonatal-lethal dilated cardiomyopathy due to a homozygous LMOD2 donor splice-site variant. >*Eur. J. Hum. Genet.* 2022 1–8 https://doi.org/10.1038/s41431-022-01043-8 (2022).
19. Greenway, S. C. et al. Early Death of 2 Siblings Related to Mutations in LMOD2, a Recently Discovered Cause of Neonatal Dilated Cardiomyopathy. *CJC Open* https://doi.org/10.1016/J.CJCO.2021.07.017 (2021).
20. Ahrens-Nicklas, R. C. et al. Disruption of cardiac thin filament assembly arising from a mutation in LMOD2: A novel mechanism of neonatal dilated cardiomyopathy. *Sci. Adv.* **5**, eaax2066 (2019).
21. Deshpande, A., Shetty, P. M. V., Frey, N. & Rangrez, A. Y. SRF: a seriously responsible factor in cardiac development and disease. *J. Biomed. Sci.* **29**, 1–21 (2022).
22. Churko, J. M. et al. Defining human cardiac transcription factor hierarchies using integrated single-cell heterogeneity analysis. *Nat. Commun.* **9**, 4906 (2018).
23. Tsukada, T. et al. Leiomodin-2 is an antagonist of tropomodulin-1 at the pointed end of the thin filaments in cardiac muscle. *J. Cell Sci.* **123**, 3136–3145 (2010).
24. Colpan, M., Iwanski, J. & Gregorio, C. C. CAP2 is a regulator of actin pointed end dynamics and myofibrillogenesis in cardiac muscle. *Commun. Biol.* **4**, 365 (2021).
25. Sala, L. et al. MUSCLEMOTION: A Versatile Open Software Tool to Quantify Cardiomyocyte and Cardiac Muscle Contraction In Vitro and In Vivo. *Circ. Res.* **122**, e5–e16 (2018).
26. Salem, T., Frankman, Z. & Churko, J. M. Tissue Engineering Techniques for Induced Pluripotent Stem Cell Derived Three-Dimensional Cardiac Constructs. *Tissue Eng. - Part B Rev.* **28**, 891–911 (2022).
27. Kolb, J. et al. Thin filament length in the cardiac sarcomere varies with sarcomere length but is independent of titin and nebulin. *J. Mol. Cell. Cardiol.* **97**, 286–294 (2016).
28. Pappas, C. T., Farman, G. P., Mayfield, R. M., Konhilas, J. P. & Gregorio, C. C. Cardiac-specific knockout of Lmod2 results in a severe reduction in myofilament force production and rapid cardiac failure. *J. Mol. Cell. Cardiol.* **122**, 88–97 (2018).
29. Treisman, R. Identification of a protein-binding site that mediates transcriptional response of the c-fos gene to serum factors. *Cell* **46**, 567–574 (1986).
30. Pellegrini, L., Tan, S. & Richmond, T. J. Structure of serum response factor core bound to DNA. *Nature* **376**, 490–498 (1995).
31. Olson, E. N. & Nordheim, A. Linking actin dynamics and gene transcription to drive cellular motile functions. *Nat. Rev. Mol. Cell Biol.* **11**, 353–365 (2010).
32. Buchwalter, G., Gross, C. & Wasylyk, B. Ets ternary complex transcription factors. *Gene* **324**, 1–14 (2004).
33. Dalton, S. & Treisman, R. Characterization of SAP-I, a Protein Recruited by Serum Response Factor to the c-fos Serum Response Element. *Cell* **66**, 597–612 (1992).
34. Hipskind, R. A., Roa, V. N., Muller, C. G. F., Raddy, E. S. P. & Nordheim, A. Ets-related protein Elk-1 is homologous to the c-fos regulatory factor p62TCF. *Nature* **354**, 531–534 (1991).
35. Zaromytidou, A.-I., Miralles, F. & Treisman, R. MAL and Ternary Complex Factor Use Different Mechanisms To Contact a Common Surface on the Serum Response Factor DNA-Binding Domain. *Mol. Cell. Biol.* **26**, 4134–4148 (2006).
36. Signaling, N., Jain, A. M. & Parmacek, M. S. Myocardin-Related Transcription Factors. *Circ. Res.* **100**, 633–644 (2007).
37. Wang, D. Z. et al. Activation of Cardiac Gene Expression by Myocardin, a Transcriptional Cofactor for Serum Response Factor. *Cell* **105**, 851–862 (2001).
38. Jeklin, A. et al. Potentiation of serum response factor activity by a family of myocardin-related transcription factors. *Corresp. álisis* **99**, 1–23 (2016).
39. Miralles, F., Posern, G., Zaromytidou, A.-I. & Treisman, R. Actin Dynamics Control SRF Activity by Regulation of Its Coactivator MAL by Rho-family small GTPases (Hill et al., 1995). Alter-ations in actin dynamics are both necessary for the acti-vation of SRF by extracellular signals and sufficient for. *Cell* **113**, 329–342 (2003).

40. Eschenhagen, T., Mummery, C. & Knollmann, B. C. Modelling sarcomeric cardiomyopathies in the dish: from human heart samples to iPSC cardiomyocytes. *Cardiovasc. Res.* **105**, 424–438 (2015).

41. Chen, X., Ni, F., Kondrashkina, E., Ma, J. & Wang, Q. Mechanisms of leiomodin 2-mediated regulation of actin filament in muscle cells. *Proc. Natl. Acad. Sci. USA.* **112**, 12687–12692 (2015).

42. Arslan, B., Colpan, M., Gray, K. T., Abu-Lail, N. I. & Kostyukova, A. S. Characterizing interaction forces between actin and proteins of the tropomodulin family reveals the presence of the N-terminal actin-binding site in leiomodin. *Arch. Biochem. Biophys.* **638**, 18–26 (2018).

43. Tolkatchev, D., Gregorio, C. C. & Kostyukova, A. S. The role of leiomodin in actin dynamics: a new road or a secret gate? *FEBS J.* **289**, 6119–6131 (2022).

44. Kurosaki, T., Popp, M. W. & Maquat, L. E. Quality and quantity control of gene expression by nonsense-mediated mRNA decay. https://doi.org/10.1038/s41580-019-0126-2.

45. Pappas, C. T., Mayfield, R. M., Dickerson, A. E., Mi-Mi, L. & Gregorio, C. C. Human disease-causing mutations result in loss of leiomodin 2 through nonsense-mediated mRNA decay. *PLOS Genet* **20**, e1011279 (2024).

46. Colpan, M. et al. Localization of the binding interface between leiomodin-2 and α-tropomyosin. *Biochim. Biophys. Acta - Proteins Proteom.* **1864**, 523–530 (2016).

47. Szatmári, D. et al. Cardiac leiomodin2 binds to the sides of actin filaments and regulates the ATPase activity of myosin. *PLoS One* **12**, e0186288 (2017).

48. Robinson, P. et al. Dilated cardiomyopathy mutations in thin-filament regulatory proteins reduce contractility, suppress systolic Ca2+, and activate NFAT and Akt signaling. *Am. J. Physiol. - Hear. Circ. Physiol.* **319**, H306–H319 (2020).

49. Reed, F., Larsuel, S. T., Mayday, M. Y., Scanlon, V. & Krause, D. S. MRTFA: A critical protein in normal and malignant hematopoiesis and beyond. *J. Biol. Chem.* **296**, 100543 (2021).

50. Le Dour, C. et al. Actin-microtubule cytoskeletal interplay mediated by MRTF-A/SRF signaling promotes dilated cardiomyopathy caused by LMNA mutations. https://doi.org/10.1038/s41467-022-35639-x.

51. Chatzifrangkeskou, M. et al. Cofilin-1 phosphorylation catalyzed by ERK1/2 alters cardiac actin dynamics in dilated cardiomyopathy caused by lamin A/C gene mutation. *Orig. Artic. Hum. Mol. Genet.* **27**, 3060–3078 (2018).

52. Guo, Y. et al. Sarcomeres regulate murine cardiomyocyte maturation through MRTF-SRF signaling. *Proc. Natl Acad. Sci. USA.* **118**, e2008861118 (2021).

53. Childers, R. C. et al. Role of the cytoskeleton in the development of a hypofibrotic cardiac fibroblast phenotype in volume overload heart failure. *Am. J. Physiol. - Hear. Circ. Physiol.* **316**, H596–H608 (2019).

54. Zeidan, A., Gan, X. T., Thomas, A. & Karmazyn, M. Prevention of RhoA activation and cofilin-mediated actin polymerization mediates the antihypertrophic effect of adenosine receptor agonists in angiotensin II- and endothelin-1-treated cardiomyocytes. *Mol. Cell. Biochem.* **385**, 239–248 (2014).

55. Zeidan, A., Javadov, S. & Karmazyn, M. Essential role of Rho/ROCK-dependent processes and actin dynamics in mediating leptin-induced hypertrophy in rat neonatal ventricular myocytes. https://doi.org/10.1016/j.cardiores.2006.06.024 (2006).

56. Hunter, J. C. et al. Nitric oxide inhibits endothelin-1-induced neonatal cardiomyocyte hypertrophy via a RhoA-ROCK-dependent pathway. *J. Mol. Cell. Cardiol.* **47**, 810–818 (2009).

57. Lai, D. et al. The Rho kinase inhibitor, fasudil, ameliorates diabetes-induced cardiac dysfunction by improving calcium clearance and actin remodeling. *J. Mol. Med.* **95**, 155–165 (2017).

58. Childers, R. C., Lucchesi, P. A. & Gooch, K. J. Decreased Substrate Stiffness Promotes a Hypofibrotic Phenotype in Cardiac Fibroblasts. *Int. J. Mol. Sci.* **22**, 6231 (2021).

59. Okamoto, R. et al. FHL2 prevents cardiac hypertrophy in mice with cardiac-specific deletion of ROCK2. *FASEB J.* **27**, 1439–1449 (2013).

60. Philippar, U. et al. The SRF target gene Fhl2 antagonizes RhoA/MAL-dependent activation of SRF. *Mol. Cell* **16**, 867–880 (2004).

61. Boateng, S. Y. & Goldspink, P. H. Assembly and maintenance of the sarcomere night and day. *Cardiovasc. Res.* **77**, 667–675 (2008).

62. Ehler, E. et al. Alterations at the Intercalated Disk Associated with the Absence of Muscle Lim Protein. *J. Cell Biol.* **153**, 763–772 (2001).

63. Müller, D. et al. How Localized Z-Disc Damage Affects Force Generation and Gene Expression in Cardiomyocytes. *Bioengineering* **8**, 213 (2021).

64. Clark, C. D. & Lee, K. H. Second heart field-specific expression of Nkx2-5 requires promoter proximal interaction with Srf. *Mech. Dev.* **162**, 103615 (2020).

65. Parlakian, A. et al. Targeted Inactivation of Serum Response Factor in the Developing Heart Results in Myocardial Defects and Embryonic Lethality. *Mol. Cell. Biol.* **24**, 5281–5289 (2004).

66. Miano, J. M. et al. Restricted inactivation of serum response factor to the cardiovascular system. *Proc. Natl Acad. Sci. USA.* **101**, 17132–17137 (2004).

67. Iwanski, J., Gregorio, C. C. & Colpan, M. Redefining actin dynamics of the pointed-end complex in striated muscle. *Trends Cell Biol.* **31**, 708–711 (2021).

68. Churko, J. M., Burridge, P. W. & Wu, J. C. Generation of Human iPSCs from Human Peripheral Blood Mononuclear Cells Using Non-integrative Sendai Virus in Chemically Defi ned Conditions. *Methods Mol. Biol.* **1036**, 81–88 (2013).

69. Littlefield, R. & Fowler, V. M. Measurement of thin filament lengths by distributed deconvolution analysis of fluorescence images. *Biophys. J.* **82**, 2548–2564 (2002).

70. Rezakhaniha, R. et al. Experimental investigation of collagen waviness and orientation in the arterial adventitia using confocal laser scanning microscopy. *Biomech. Model. Mechanobiol.* **11**, 461–473 (2012).

71. Szklarczyk, D. et al. STRING v11: Protein-protein association networks with increased coverage, supporting functional discovery in genome-wide experimental datasets. *Nucleic Acids Res.* **47**, D607–D613 (2019).

72. Heinz, S. et al. Article Simple Combinations of Lineage-Determining Transcription Factors Prime cis-Regulatory Elements Required for Macrophage and B Cell Identities. https://doi.org/10.1016/j.molcel.2010.05.004 (2010).

73. Brand, N. J., Lara-Pezzi, E., Rosenthal, N. & Barton, P. J. R. Analysis of cardiac myocyte biology in transgenic mice: a protocol for preparation of neonatal mouse cardiac myocyte cultures. *Methods Mol. Biol.* **633**, 113–124 (2010).

74. Bolsover, S., Ibrahim, O., O'luanaigh, N., Williams, H. & Cockcroft, S. Use of fluorescent Ca 2 + dyes with green fluorescent protein and its variants: problems and solutions. *Biochem. J.* **356**, 345–352 (2001).

75. Farman, G. P., Walker, J. S., de Tombe, P. P. & Irving, T. C. Impact of osmotic compression on sarcomere structure and myofilament calcium sensitivity of isolated rat myocardium. *Am. J. Physiol. Circ. Physiol.* **291**, H1847–H1855 (2006).

76. Mudry, R. E., Perry, C. N., Richards, M., Fowler, V. M. & Gregorio, C. C. The interaction of tropomodulin with tropomyosin stabilizes thin filaments in cardiac myocytes. *J. Cell Biol.* **162**, 1057–1068 (2003).

Author contributions

Conceptualization, J.B.I., C.T.P., and C.C.G.; methodology, J.B.I., C.T.P., J.M.C., R.M.M., and G.P.F.; validation J.B.I., C.T.P., R.M.M. and J.M.C.; formal analysis J.B.I., C.T.P., G.P.F. and J.M.C.; resources, C.C.G., R.A.N., and J.M.C.; writing- original draft J.B.I., and C.T.P.; writing-review & editing, C.T.P., C.C.G., R.M.M., G.P.F., R.A.N., and J.M.C.; visualization, J.B.I., C.T.P. and J.M.C.; supervision J.M.C. and C.C.G., funding acquisition J.M.C. and C.C.G. All authors read and approved the final manuscript.

Competing interests

The authors declare no competing interests.

Additional information

Supplementary information The online version contains supplementary material available at https://doi.org/10.1038/s41536-024-00366-y.

Correspondence and requests for materials should be addressed to Jared M. Churko or Carol C. Gregorio.

Reprints and permissions information is available at http://www.nature.com/reprints

Publisher's note Springer Nature remains neutral with regard to jurisdictional claims in published maps and institutional affiliations.